

# Rejuvenation of Directionally Solidified and Single-Crystal Nickel-Base Superalloys



L.H. RETTBERG, P.G. CALLAHAN, B.R. GOODLET, and T.M. POLLOCK

During service, superalloy turbine components degrade over time by creep and fatigue deformation mechanisms due to a complex combination of stresses at high temperatures. The high cost of fabricating Ni-base superalloy components and, consequently, replacement components has encouraged the development of rejuvenation (restoration) procedures to extend useful service life. The processes that limit repeated rejuvenation of directionally solidified GTD444 and single-crystal René N5(SX) alloys have been studied in detail. A rejuvenation cycle includes a rejuvenation heat treatment and/or small-scale material removal, followed by creep or fatigue testing. With the application of multiple rejuvenation cycles, the total creep rupture life of René N5(SX) tested at 982 °C and 206 MPa was extended by a factor of 2.8 over the baseline rupture life. To produce this increase in rupture life, creep strains were limited to 2 or 3 pct prior to application of a rejuvenation cycle, involving solutioning at 28 °C below the  $\gamma'$  solvus temperature for 2 hours and aging at 1079 °C for 4 hours. Rejuvenation of compressive hold-time fatigue damage was also successful with the use of small-scale material removal. Due to the tortuosity of the grain boundaries in GTD444(DS), some boundaries are initially oriented transverse to the growth direction. The enhanced plasticity near these grain boundaries may be the primary reason why the initially single-crystal René N5(SX) specimens were more amenable to rejuvenation than GTD444(DS). For both alloys, recrystallization after multiple rejuvenation cycles was responsible for early failure during the subsequent creep test. Resonant ultrasound spectroscopy was successfully implemented to detect the presence of recrystallized grains.

<https://doi.org/10.1007/s11661-021-06150-7>

© The Minerals, Metals & Materials Society and ASM International 2021

## I. INTRODUCTION

IN service, superalloy turbine blades experience local degradation due to creep, fatigue, and oxidation, leading to their replacement with new components. The high cost of the original Ni-base superalloy components and, consequently, replacement components has encouraged the development of rejuvenation (restoration) procedures to repair turbine blades and extend useful service life. This is especially important for land-based gas turbine engines, where a single turbine blade (up to 40 lbs) can cost tens of thousands of dollars, due to investment casting, coatings, machining, the use of alloys with relatively rare elements such as Re, and overall size of the component.

Previous studies on rejuvenation have employed complex heat treatments in order to restore creep behavior.<sup>[1–12]</sup> If creep cavities or cracks were present, then hot isostatic pressing (HIP) was also required to extend creep life. However, a number of studies were conducted such that tests were interrupted prior to the formation of creep cavities or cracks to avoid using HIP.<sup>[1–4]</sup>

There have been limited studies on the rejuvenation of DS and SX superalloys. One study, conducted by Ross *et al.*, examined multiple rejuvenation of Mar-M200 + Hf(DS). Creep testing was performed at 982 °C/172 MPa and interrupted at every 1 pct strain. Multiple rejuvenation was successful up to a total creep strain of 3 pct, after which the minimum creep rate increased and the time to an additional 1 pct strain significantly decreased.<sup>[5]</sup> Surface cracking, detected by visual and fluorescent penetrant inspections, was believed to be the cause of the loss of creep properties. Rejuvenation of the single-crystal Ni-base superalloy (SX) ERBO/1 was examined by Rutttert *et al.*<sup>[11]</sup> Creep was performed at 1050 °C/160 MPa, and a multistep supersolvus HIP rejuvenation heat treatment was used. A specimen was crept to 1.5 pct strain and the rejuvenation heat treatment resulted in improved creep

L.H. RETTBERG, P.G. CALLAHANA, B.R. GOODLETA, and T.M. POLLOCKA are with the Materials Department, University of California, Santa Barbara, Bldg. 503, Rm. 1355, Santa Barbara, CA, 93106-5050. Contact e-mail: luke.rettberg@gmail.com

Manuscript submitted September 15, 2018, accepted January 3, 2021.

Article published online March 21, 2021

behavior during the subsequent creep test. In addition, Yao *et al.* noted chemical segregation after long-term thermal exposures of CMSX-4(SX) specimens influencing the creep performance of post-rejuvenated specimens.<sup>[12]</sup>

Repair procedures have also been applied to specimens machined from service-exposed DS turbine blades. Lamberigts *et al.* performed repair procedures on specimens machined from Mar-M-200 + Hf(DS) turbine blades.<sup>[10]</sup> Service damage was simulated by performing stress-rupture tests. HIP at a temperature near the  $\gamma'$  solvus (1230 °C), followed by full solutioning and aging, was used to completely heal  $\gamma'$  rafting and incipient melting. The performance of rejuvenated specimens fell within the experimental scatter of pre-crept specimens. Kuipers *et al.* performed various rejuvenation heat treatments on René N5(SX) and RR2000(SX).<sup>[13]</sup> The authors observed cellular recrystallization after applying the rejuvenation heat treatment in areas of the blades where prior peening had induced residual stresses. A long-term annealing heat treatment prior to rejuvenation was unable to prevent recrystallization.

Figure 1 schematically demonstrates the benefit of rejuvenation to creep life and highlights the importance of understanding the damage mechanisms that result in tertiary creep and quantification of which types of damage are recoverable. Tertiary creep damage in GTD444(DS) and René N5(SX) is most likely a combination of several different mechanisms. Based on the previous work on creep of nickel-base alloys, it is hypothesized that the dominant tertiary creep damage mechanism is at least initially related to rafting, shearing of the  $\gamma'$ , and an increase in the mobile dislocation density.<sup>[14]</sup> Unfortunately, the individual contributions of microstructural instability and damage in the form of voids and cracks have not yet been studied in detail for DS and SX superalloys. The non-recoverable forms of damage in fatigue are also not well understood.

A particularly detrimental form of fatigue occurs during cycling with extended holds in compression. Referred to as sustained-peak low-cycle fatigue (SPLCF), cracks form at the surface and oxidation of

the open crack faces occurs, creating a growth strain that induces a compressive growth stress within the  $\alpha$ -Al<sub>2</sub>O<sub>3</sub> thermally grown oxide (TGO). The growth strain arises from oxidation on the transverse grain boundaries of the TGO.<sup>[15,16]</sup> The local in-plane compressive stress on the surface of the blades causes transverse out-of-plane extension of the substrate (Poisson effect) into the TGO-lined crack.<sup>[17]</sup> Cracks extend by the effective growth of the TGO and are accommodated by substrate creep. This process becomes more complicated in multilayer systems, where the oxidation kinetics and growth strains will vary with the crack location.<sup>[18]</sup> Similar to creep testing, rafting of the  $\gamma'$  precipitates also occurs.

Given the overall limited number of studies on rejuvenation in polycrystalline materials, with even fewer studies on advanced materials, additional study is warranted. The research discussed in this paper is focused on recovering both creep and fatigue properties, and presents the results of a multiple rejuvenation test procedure. Discussion is provided on the feasibility of using rejuvenation to extend service life of directionally solidified (DS) and single-crystal (SX) Ni-base superalloys based on the underlying rejuvenation limiting mechanisms.

## II. MATERIALS AND METHODS

The superalloy material, provided by GE Power & Water, consisted of GTD444(DS) and René N5(SX) 24 × 13 × 1.5 cm Bridgman cast plates that were solutioned and aged with standard commercial cycles prior to machining. Nominal compositions are shown in Table I. Special care was taken to minimize surface residual stresses in the creep and fatigue specimens by machining with a low stress grinding processes. The rationale for using creep and fatigue tests to induce damage is based on the reported service limiting deformation mechanisms.<sup>[19]</sup> The major chemical differences between GTD444(DS) and René N5(SX) include the absence of Ti and addition of Re in René N5(SX) along with lower levels of the grain boundary strengtheners carbon and boron. The approximate gamma prime solvi are between 1250 °C and 1300 °C for GTD444(DS) and René N5(SX).

### A. Creep Testing

Creep tests were performed under constant load in air at two conditions, depending on the alloy: 982 °C/179 MPa for GTD444(DS) and 982 °C/206 MPa for René N5(SX) specimens. Initial creep specimens were tested to rupture, and subsequent tests were interrupted at 2, 5, 10, and 20 pct creep strain to examine the microstructural evolution and damage as a function of strain. All GTD444(DS) and René N5(SX) creep specimens tested were machined and consequently crept along the nominally [001] crystal direction within a 15 deg tolerance. Interrupted creep tests were allowed to cool under load before being unloaded and removed from the creep frame. For each creep test, the load was adjusted based

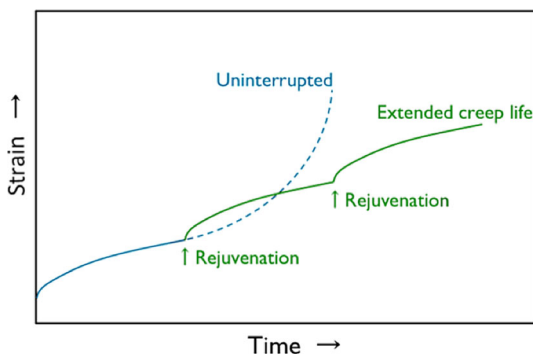


Fig. 1—Schematic adapted from Maccagno *et al.* illustrating the expected result (green line) from a successful multiple rejuvenation creep test compared to an uninterrupted creep test (blue line).<sup>[7]</sup> In this illustration, successful rejuvenation is defined by a longer total creep life when compared to an uninterrupted test (Color figure online).

**Table I. Composition, in Weight Percent, of the DS and SX Gas Turbine Alloys Investigated in This Study**

	Cr	Co	Mo	W	Ta	Nb	Al	Ti	Hf	Re	Ni	References
GTD444(DS)	9.7	8	1.5	6	4.7	0.5	4.2	3.5	0.15	—	bal.	38
René N5(SX)	7	7.5	1.5	5	6.5	—	6.2	—	0.15	3	bal.	39,40

on the specimen diameter. Baseline creep tests for both GTD444(DS) and René N5(SX) can be found in Rettberg *et al.*<sup>[20]</sup>

### B. Sustained-Peak Low-Cycle Fatigue Testing

SPLCF testing was conducted on bare René N5(SX). The specimens were tested along the [001] crystal direction within a 15 deg tolerance at a constant temperature of 982 °C in air with a strain range of 0.6 pct and  $R = -\infty$  ( $A = -1.0$ ). The testing waveform consisted of a 120 seconds compressive hold followed by a 3 seconds loading–unloading cycle. The number of cycles to failure was defined by a 25 pct tensile load drop from the stabilized value.

A grinding and polishing procedure was performed on the fatigue specimens with the specimens mounted in a drill press following standard procedures. A final polishing step of 3  $\mu\text{m}$  diamond was used to minimize the influence of surface topography on the crack initiation process.

### C. Microstructural Analysis

The microstructure was examined for both alloys after creep and fatigue testing to determine the onset of recrystallization, extent of rafting, formation of cavities or voids, changes in carbide morphology, and precipitation of brittle intermetallic phases. The results were compared to the pre-crept microstructure. Metallographic preparation of pre-crept and crept specimens involved mounting sections parallel and transverse to the stress axis in Bakelite, followed by standard grinding and polishing with a final polish of 0.05  $\mu\text{m}$  alumina. Sections were cut *via* electrical discharge machining (EDM), and specimens were ultrasonically cleaned after each polishing step in distilled water.

Two etchants were used to inspect the microstructure: 40 pct hydrochloric acid, 40 pct ethylene glycol, and 20 pct nitric acid for macroetching of GTD444(DS); 33 pct distilled water, 33 pct acetic acid, 33 pct nitric acid, and 1 pct hydrofluoric acid for microetching of GTD444(DS) and René N5(SX). Electron backscatter diffraction (EBSD) was performed using an FEI® (Hillsboro, Oregon) XL30 field emission gun (FEG) scanning electron microscope (SEM). EBSD was used to determine the crystal orientation and, with subsequent data analysis, the local misorientation by calculation of the kernel average misorientation (KAM) and grain orientation spread (GOS), through which the presence or absence of both dynamic and static recrystallization was determined.

### D. Heat Treatments

Coupons were cut from specimens of GTD444(DS) and René N5(SX) that were crept to 2 and 5 pct strain for initial rejuvenation heat treatment studies. Virgin coupons were also heat treated to determine the influence of strain on the dissolution, reprecipitation, and growth of the  $\gamma'$  phase. The heat treatment conditions are summarized in Table II with only the solution temperature being changed between experimental variants.

## III. DESIGN OF A REJUVENATION PROCEDURE

A rejuvenation heat treatment is capable of reducing the dislocation density by recovery and dissolving the  $\gamma'$  rafts into solution. Reprecipitation of cuboidal  $\gamma'$  precipitates will occur during cooling from the rejuvenation heat treatment temperature. Consequently, it is hypothesized that in order to recover the virgin creep properties and extend creep life, a rejuvenation heat treatment will be required only if  $< 5$  pct creep strain has been accumulated.

### A. Rejuvenation Heat Treatment: Creep

To test the effectiveness of a rejuvenation heat treatment in restoring the original microstructure at various solution temperatures and creep strain levels, initial heat treatment studies were performed on coupons cut from creep specimens of GTD444(DS) and René N5(SX) crept to 2 pct and 5 pct strain. The damage observed up to 5 pct strain during high temperature (982 °C) and low stress (172–206 MPa) creep of GTD444 and René N5(SX) consisted of an increase in the dislocation density and rafting of the  $\gamma'$  phase.<sup>[20]</sup> Virgin coupons were also heat treated to determine the influence of strain on the dissolution, reprecipitation, and growth of the  $\gamma'$  phase. The heat treatment conditions are summarized in Table II. Heating and cooling rates were chosen to meet typical industry specifications and were performed in either vacuum or a 5 pct H<sub>2</sub>/Ar reducing atmosphere. Representative micrographs for each alloy after heat treatment are shown in Figures 2 through 5.

As the solution temperature was decreased below the  $\gamma'$  solvus, the volume fraction of unsolved phases in GTD444(DS) increased regardless of initial condition, Figure 2. Similar results were observed for heat-treated René N5(SX) coupons. When examining the  $\gamma'$  morphology in the dendrite core regions, the lowest solution temperature used for GTD444(DS) of 28 °C below the  $\gamma'$

solvus was unable to dissolve all of the rafted precipitates, Figure 3. Thus, of the solution temperatures used in this study, the minimum temperature capable of at least partially recovering the initial  $\gamma'$  morphology for GTD444(DS) is 14 °C below the  $\gamma'$  solvus. For René N5(SX), the rafted structure was successfully eliminated at solution temperatures equal to and above 56 °C below the  $\gamma'$  solvus. After aging, the  $\gamma'$  size has increased, and a cuboidal morphology is achieved for both alloys, see Figures 4 and 5. It is worth noting that as the solution temperature is decreased, the  $\gamma'$  morphology becomes less cuboidal; this is especially evident in GTD444(DS).

## B. Quantitative Microstructural Analysis

In order to quantify the microstructural differences due to mechanical testing and rejuvenation, moment invariants (MI) are used to characterize the  $\gamma'$  precipitate morphology. MI have been used previously in the literature to successfully characterize 2D- and 3D-phase field-generated precipitates and to characterize simulated rafted microstructures for superalloys.<sup>[21–23]</sup>

The MI of interest are second-order and fourth-order moments that are invariant with respect to affine and similarity transformations. They are also central moments, meaning that each object has been translated so that the center of mass is located at the origin. Micrographs are first segmented using an algorithm that fills shapes based on an edge map before the MI can be calculated. The segmentation process is outlined in Figure 6. Equation [1] is used to calculate each object's moment invariants at coordinates  $(x, y)$  with respect to the object's center of mass at coordinates  $(x_c, y_c)$ . The order of the MIs,  $n$ , is equal to  $p + q$ .

$$\bar{\mu}_{pq} \equiv \int \int_D dx dy (x - x_c)^p (y - y_c)^q. \quad [1]$$

The two second-order MIs used for this study are referred to as  $\omega_1$  and  $\omega_2$  (see Eqs. [2] and [3]), respectively. The MIs have been normalized by a factor of the object's surface area,  $A = \mu_{00}$ , so that  $0 \leq \omega_i \leq 1$ .

$$\omega_1 \equiv \frac{A^2}{2\pi(\bar{\mu}_{20} + \bar{\mu}_{02})}; \quad [2]$$

$$\omega_2 \equiv \frac{A^2}{16\pi^2(\bar{\mu}_{20}\bar{\mu}_{02} + \bar{\mu}_{11}^2)}. \quad [3]$$

Area-weighted averages of the fourth-order moments,  $\tau_1$ ,  $\tau_2$ , and  $\tau_3$ , were also calculated and are analogous to the kurtosis, which for the case of a 1D distribution describes the peakedness. The second-order and fourth-order MI are listed in Table III for the coupon heat treatment studies performed. The precipitates used to calculate the MI were from the dendritic core regions of René N5(SX) specimens. At solution temperatures greater than or equal to 14 °C below the  $\gamma'$  solvus, no trend was evident in the MI as a function of prior creep

strain. However, at solution temperatures less than and equal to 28 °C below the  $\gamma'$  solvus, all of the calculated second- and fourth-order MI decreased as the prior creep strain increased. Thus, a more complex precipitate shape was present after heat treatments in specimens with higher levels of creep strain at lower solution temperatures when compared to the baseline 0 pct strain coupon. If the average precipitate shape was a perfect square, the normalized MI would have approximate values of 0.940 for  $\omega_i$  and 0.800 for  $\tau_i$ . As expected, the quantitative precipitate shape analysis indicated that at higher solution temperatures, a rejuvenation heat treatment is more capable of recovering the microstructure to the baseline precipitate shape up to a creep strain of 5 pct.

## C. Rejuvenation Heat Treatment and Material Removal: Fatigue

In addition to recovering creep properties, fatigue damage must also be addressed for complete repair of common service damage. The challenge with fatigue rejuvenation is apparently a direction result of the inability of simple rejuvenation heat treatments and even HIP (in the case of oxidized cracks) to remove the dominant form of damage, surface fatigue cracks. It was hypothesized that interrupting SPLCF tests at 50 pct of expected life and then grinding and polishing away material to a sufficient depth to remove any surface cracks present and applying a subsequent rejuvenation heat treatment should recover the fatigue properties. Successful recovery of fatigue properties will depend on the removal of the deepest surface cracks, because these cracks will most likely cause early failure upon retesting. Due to the fact that cracks initiate at the surface, their complete removal was verified by optical microscopy.

## D. Defining a Rejuvenation Cycle

In order to determine the success of the repair/rejuvenation procedures and to elucidate the processes that prevent successful rejuvenation, repeated rejuvenation cycles have been performed. A rejuvenation cycle includes rejuvenation heat treatment and/or small-scale material removal of a surface layer, followed by creep or fatigue (SPLCF) testing, as presented schematically in Figure 7. Multiple rejuvenation testing is defined in this context as the application of repeated rejuvenation cycles until specimen failure. Prior to initial testing, the fatigue and creep specimens are polished to 3  $\mu\text{m}$  diamond in order to remove surface damage caused by machining and heat treated at the same conditions as the rejuvenation heat treatment to establish a relevant mechanical behavior baseline.

Creep testing was repeatedly interrupted at various creep strain thresholds (2, 3, or 5 pct) to investigate the influence of strain, while SPLCF tests were only interrupted at 50 pct of expected life. Coated René N5(SX) specimens were also tested at a single-creep strain threshold of 2 pct. Only one SPLCF threshold was used due to the ease of using non-destructive evaluation (visual surface inspection) to confirm the



**Table II. Summary of the Rejuvenation Heat Treatments Performed on 2 pct Crept, 5 Pct Crept, and Virgin Coupons of GTD444 and René N5(SX)**

	Solution Temp.	Time (h)	Aging Temp. (°C)	Time (h)
GTD444(DS)	full $\gamma'$ solvus	2	1079	4
	14 °C below solvus	2	1079	4
	28 °C below solvus	2	1079	4
René N5(SX)	full $\gamma'$ solvus	2	1079	4
	14 °C below solvus	2	1079	4
	28 °C below solvus	2	1079	4
	42 °C below solvus	2	1079	4
	56 °C below solvus	2	1079	4

The only difference between heat treatments was the solution temperature, which was at either the  $\gamma'$  solvus temperature or a multiple of 14 °C below the full  $\gamma'$  solvus temperature.

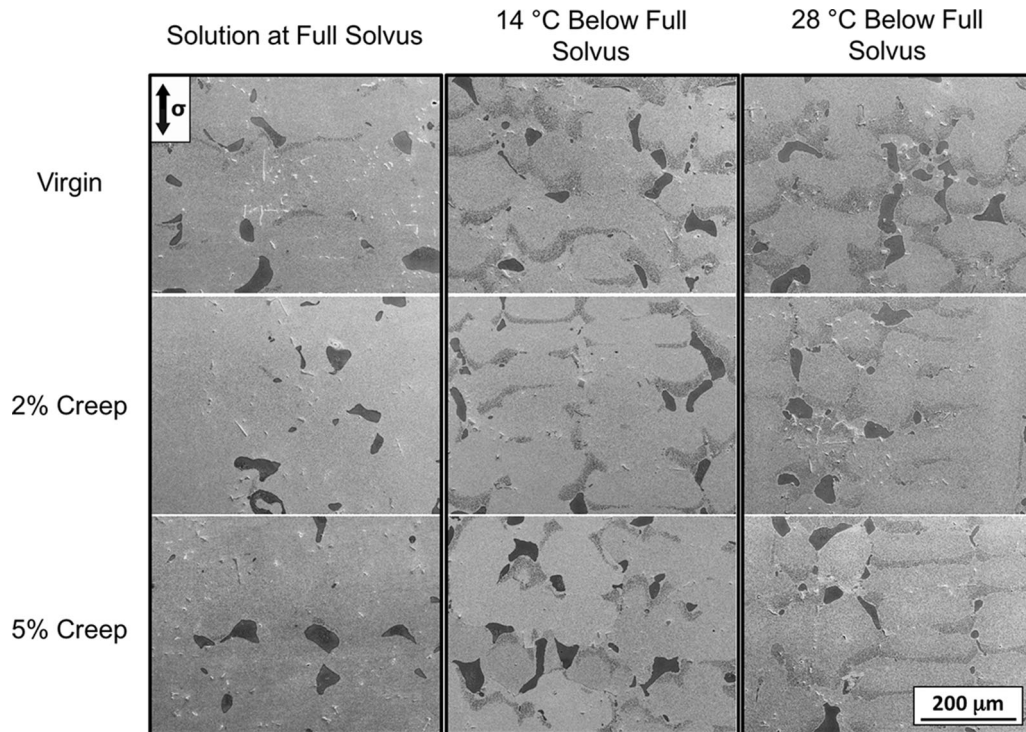


Fig. 2—Low-magnification micrographs collected from solution-treated coupons of GTD444(DS). Notice the volume fraction of unsolved phases increases as the solution temperature is decreased from the  $\gamma'$  solvus. All solution heat treatments were held at temperature for 2 h.

complete removal of fatigue cracks. Interrupting SPLCF tests at a higher or lower fraction of expected life would only change the amount of polishing required. These thresholds were chosen based on the observed damage in the interrupted testing, specifically the measured length of fatigue cracks during SPLCF testing and the absence of carbide cracking and growth of existing solidification pores during creep to 5 pct strain.<sup>[24]</sup>

Non-destructive evaluation (NDE) techniques have been implemented in the multiple rejuvenation cycle after each rejuvenation heat treatment and mechanical test to investigate their usefulness in determining the presence of non-recoverable damage. In this investigation, multiple rejuvenation cycles were conducted until failure; thus, the only way to detect the presence and evolution of non-recoverable damage *in situ* is through the use of NDE. Non-recoverable damage includes

recrystallization, cracks, and cavities. Besides standard visual surface inspection to detect cracks, resonant ultrasound spectroscopy (RUS) was also used. For a discussion of the fundamentals of RUS and an example of successful detection of recrystallization in DS superalloys, the reader is referred to a manuscript by Rettberg *et al.*<sup>[25]</sup>

#### E. Rejuvenation Heat Treatment Parameters

Based on the coupon heat treatment results for GTD444(DS), a rejuvenation heat treatment solution temperature of 14 °C below the  $\gamma'$  solvus was used for multiple rejuvenation creep testing. At this temperature, restoration of the cuboidal  $\gamma'$  morphology occurs; however, some of the original  $\gamma'$  precipitates remain in

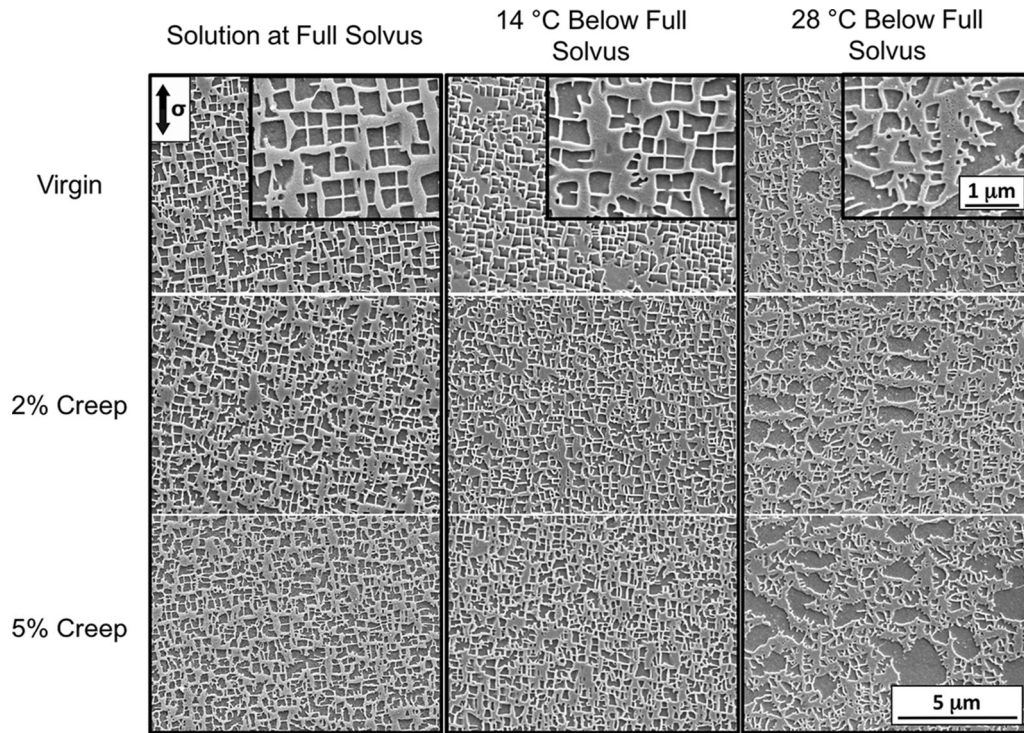


Fig. 3—High-magnification micrographs collected from the dendrite core regions of solution-treated coupons of GTD444(DS). Solution heat treatments were held at temperature for 2 h. Dissolution of the  $\gamma'$  phase did not occur in dendrite core regions at a solution temperature 28 °C below the  $\gamma'$  solvus temperature.

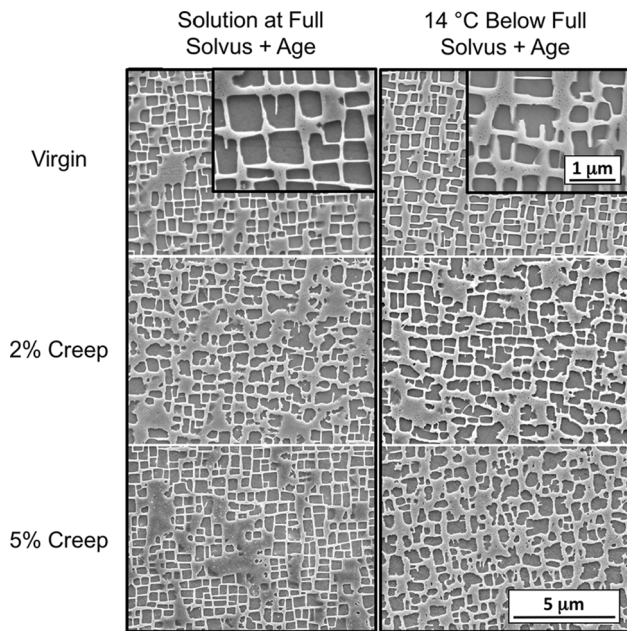


Fig. 4—A comparison of the resulting microstructure after a solution + age heat treatment of GTD444(DS). Images were collected from the dendrite core regions of the microstructure.

the interdendritic regions during the rejuvenation heat treatment.

For René N5(SX), solutioning was performed at the  $\gamma'$  solvus, 28 °C, and 42 °C below the  $\gamma'$  solvus. A range of

solution temperatures was explored due to the overall higher  $\gamma'$  solvus, a result of the increased  $\gamma'$  solute content in René N5(SX) compared to GTD444(DS). The addition of Ta not only increases the  $\gamma'$  stability but also, due to the strong tendency for Ta to segregate to the interdendritic regions of the microstructure, will lead to an increase in the difference between the dendrite core and interdendritic  $\gamma'$  solvi.<sup>[14]</sup>

The purpose of lowering the solution heat treatment temperature is to retain  $\gamma'$  precipitates in the interdendritic regions of the microstructure, which provide a substantial barrier to recrystallization. Recrystallization nuclei are expected to preferentially form in the interdendritic regions due to the presence of stress concentrators, such as carbides and solidification porosity; retained  $\gamma'$  precipitates in these regions can pin the recrystallization nuclei, suppressing their growth. Over time, recrystallization nuclei will also form in the dendrite cores and near the specimen surface aided by the depletion of  $\gamma'$  formers via oxidation; thus, recrystallization is not expected to be suppressed indefinitely.

Each rejuvenation heat treatment included a 2 hours hold at the solution temperature followed by a 4 hours aging treatment at 1079 °C. The cooling rate from the solution temperature was consistent between all rejuvenation heat treatments and was chosen based on industrial standards. The success of applying each multiple rejuvenation cycle based on subsequent mechanical testing will be discussed in the next section for both GTD444(DS) and René N5(SX).



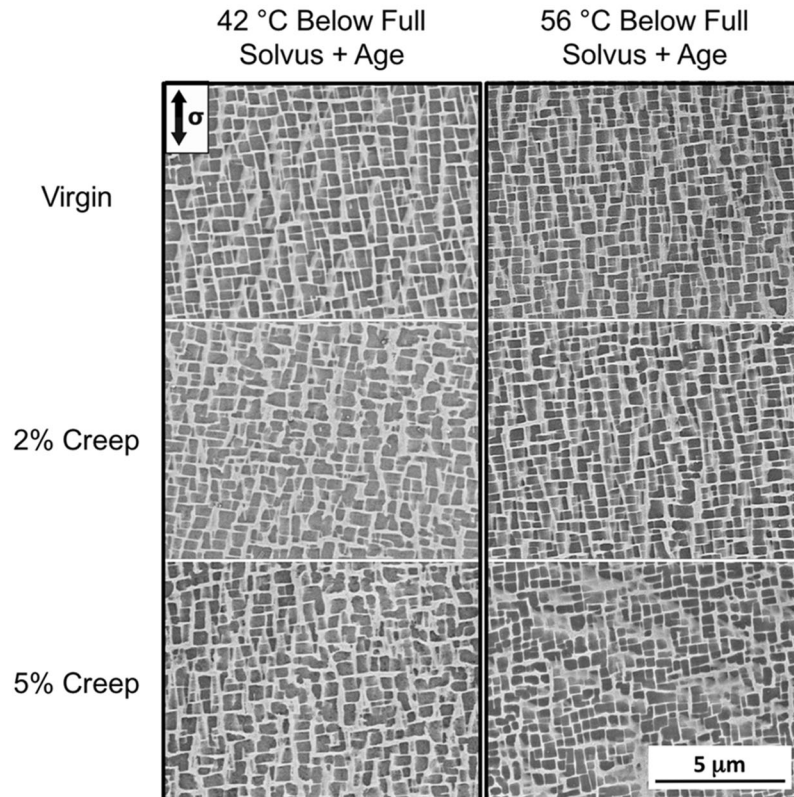
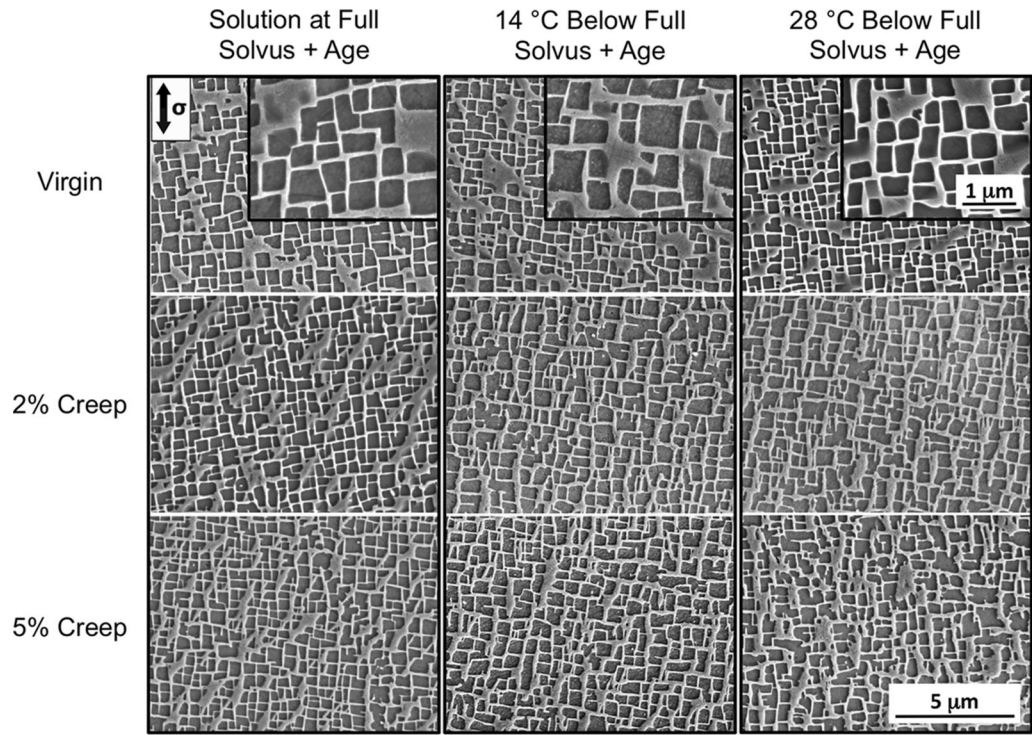


Fig. 5—Micrographs of the René N5(SX) microstructure after a solution + age heat treatment at various creep strains and solution temperatures. Images were collected from the dendrite core regions of the microstructure.

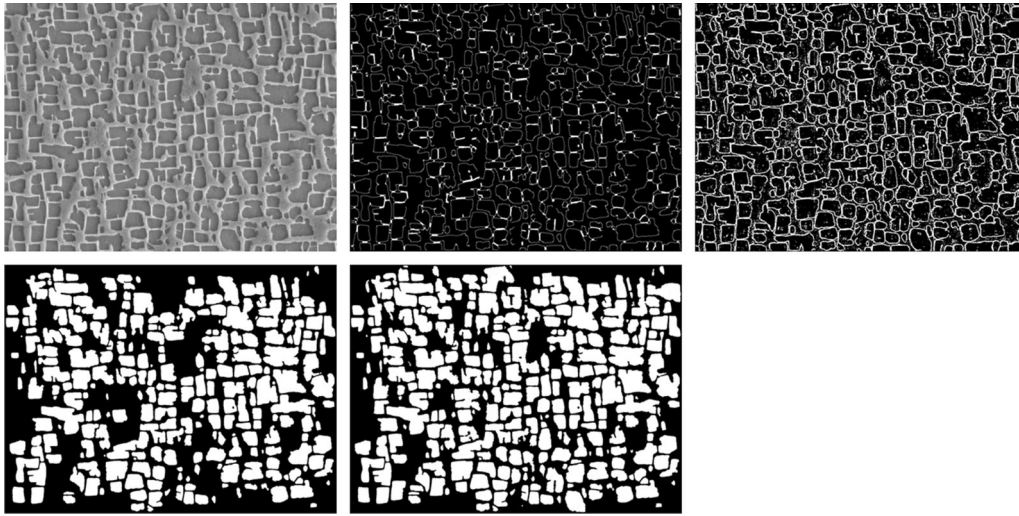


Fig. 6—Representative images outlining the segmentation process from top left to the bottom right that creates a binary image of white  $\gamma'$  precipitates and a black  $\gamma$  matrix for subsequent calculation of the moment invariants. From the original micrograph, edges are determined and the precipitates are filled. Manual adjustment is required in some situations to capture all of the  $\gamma'$  precipitates (with edge precipitates being ignored).

#### IV. LIFE EXTENSION VIA THE APPLICATION OF MULTIPLE REJUVENATION CYCLES

The multiple rejuvenation test conditions are summarized in Table IV and, henceforth, each test will be referred to by the corresponding label.

##### A. Multiple Rejuvenation: Creep of René N5(SX)

Creep tests of René N5(SX) specimens were performed to the desired creep strain threshold (either 2, 3, or 5 pct strain) followed by a rejuvenation heat treatment, with NDE before and after each mechanical test and heat treatment. This defined one complete rejuvenation cycle, which was repeated until failure; thus, indefinite rejuvenation was not observed. The rejuvenation heat treatments were applied to full, intact creep specimens and, to isolate the influence of the creep strain threshold, solutioning during rejuvenation heat treatments was only performed at a temperature of 28 °C below the  $\gamma'$  solvus. This solution temperature was chosen as a starting point, with the ultimate goal of suppressing recrystallization, as discussed in Section III-E, while also partially restoring the initial cuboidal  $\gamma'$  microstructure. All creep tests for René N5(SX) specimens were performed at 982 °C/206 MPa.

##### 1. Influence of the Creep Strain Threshold: René N5(SX)

Creep curves from the multiple rejuvenation test N5-28-5 are shown in Figure 8 with each creep segment and rejuvenation heat treatment labeled. Three creep tests and two rejuvenation heat treatments were performed before specimen rupture occurred. The total creep life to failure of 305 hours was lower than the baseline rupture life of 344 hours. There was also a decrease in creep rupture ductility to 18 pct strain

compared to the baseline of 35 pct. The time to 5 pct creep strain was reduced by 70 pct between the first (CT1) and second (CT2) creep tests, as shown in Figure 8(b) and listed in Table V. In addition, the minimum creep rate for the second creep test increased by a factor of 4 compared to the first test. Thus, rejuvenating specimens after every 5 pct creep strain was not successful, leading to a lower total rupture life and an increased minimum creep rate. Due to unsuccessful rejuvenation, the third creep test (CT3) was not interrupted and the test continued until rupture.

Multiple rejuvenation tests at lower creep strain thresholds of 2 and 3 pct creep strain (tests N5-28-2 and N5-28-3) resulted in total creep lives of 952 and 951 hours, compared to the baseline of 344 hours and creep rupture strains of 12 and 15 pct, respectively. At both 2 pct and 3 pct strain, after the first creep test (CT1), a decrease in creep performance was observed. This was evident in both the time to the creep strain threshold and in the minimum creep rate for the second creep test (CT2), as shown in Figure 9. However, each subsequent creep test maintained a similar minimum creep rate and time to the creep strain threshold. Due to the factor of 2.8 increase in the creep rupture life for both the 2 and 3 pct creep strain threshold tests and a stable minimum creep rate, rejuvenation was considered to be successful.

Characterization of the specimens via EBSD after failure led to the discovery of recrystallization, which occurred during the rejuvenation heat treatments, Figure 10. Recrystallization was observed in all specimens tested (2, 3, and 5 pct strain threshold tests), and cracking occurred along the grain boundaries of the recrystallized grains that were oriented transverse to the loading direction. It is assumed that a majority of these surface cracks formed during subsequent creep testing following recrystallization that occurred during the previous rejuvenation heat treatment. The entire



**Table III. Table Listing the Second-Order ( $\omega_1$  and  $\omega_2$ ) and Fourth-Order ( $\tau_1$ ,  $\tau_2$ , and  $\tau_3$ ) Moment Invariants from Micrographs of Crept and Subsequently Heat-treated René N5(SX) Specimens**

Solution Temp.	Creep Strain (Pct)	$\omega_1$	$\omega_2$	$\tau_1$	$\tau_2$	$\tau_3$
Full Solvus	0	0.851	0.854	0.675	0.639	0.638
	2	0.835	0.857	0.647	0.662	0.634
	5	0.843	0.858	0.659	0.649	0.634
- 14 °C	0	0.843	0.865	0.666	0.666	0.658
	2	0.801	0.815	0.598	0.603	0.569
	5	0.802	0.836	0.601	0.626	0.600
- 28 °C	0	0.839	0.862	0.658	0.664	0.667
	2	0.793	0.813	0.588	0.603	0.574
	5	0.772	0.797	0.550	0.570	0.522
- 42 °C	0	0.852	0.874	0.685	0.697	0.682
	2	0.783	0.809	0.568	0.603	0.556
	5	0.763	0.798	0.547	0.589	0.547
- 56 °C	0	0.825	0.871	0.642	0.685	0.683
	2	0.817	0.864	0.627	0.684	0.669
	5	0.762	0.798	0.546	0.584	0.543

Coupon solution heat treatments were performed at either the full  $\gamma'$  solvus temperature or at a multiple of 14 °C below the full  $\gamma'$  solvus temperature with all specimens being aged at 1079 °C for 4 h.

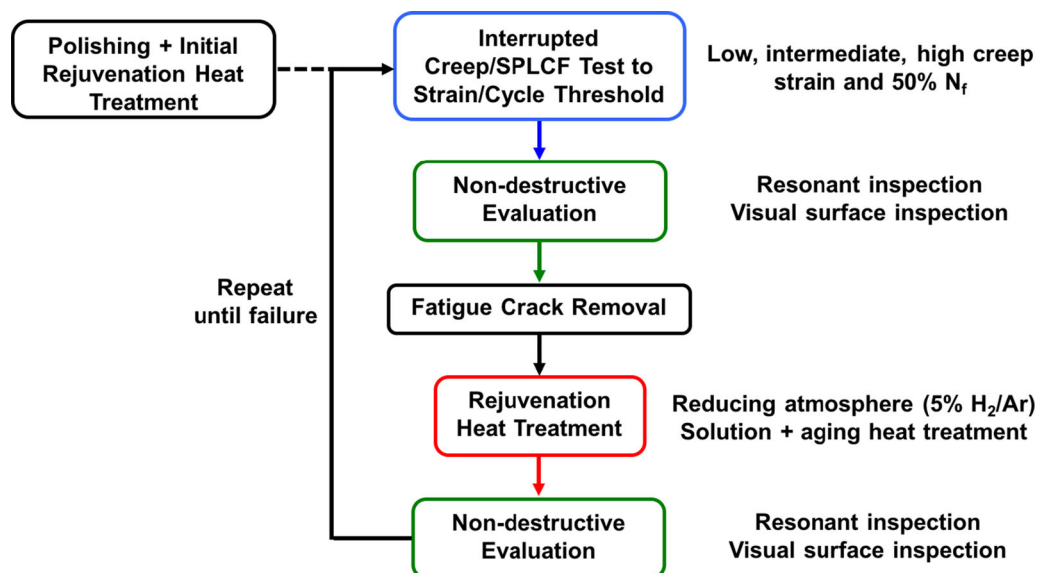


Fig. 7—Schematic outlining the multiple rejuvenation testing procedure used for both GTD444(DS) and René N5(SX). The fatigue crack removal is only performed during multiple rejuvenation of SPLCF test specimens.

**Table IV. Table Listing All of the Multiple Rejuvenation Creep Tests Performed**

	Label	Solution Temp.	Creep Strain Threshold (Pct)
GTD444(DS)	444-14-1	14 °C below solvus	1
	444-14-2a	14 °C below solvus	2
	444-14-2b	14 °C below solvus	2
	444-14-3	14 °C below solvus	3
René N5(SX)	N5-FS-2	full $\gamma'$ solvus	2
	N5-28-2	28 °C below solvus	2
	N5-56-2	56 °C below solvus	2
	N5-28-3	28 °C below solvus	3
	N5-28-5	28 °C below solvus	5
	N5-28-2-CT	28 °C below solvus	2

Label convention: alloy type -°C below the  $\gamma'$  solvus or at the full solvus (FS) - creep strain threshold value (pct) - coated (CT).

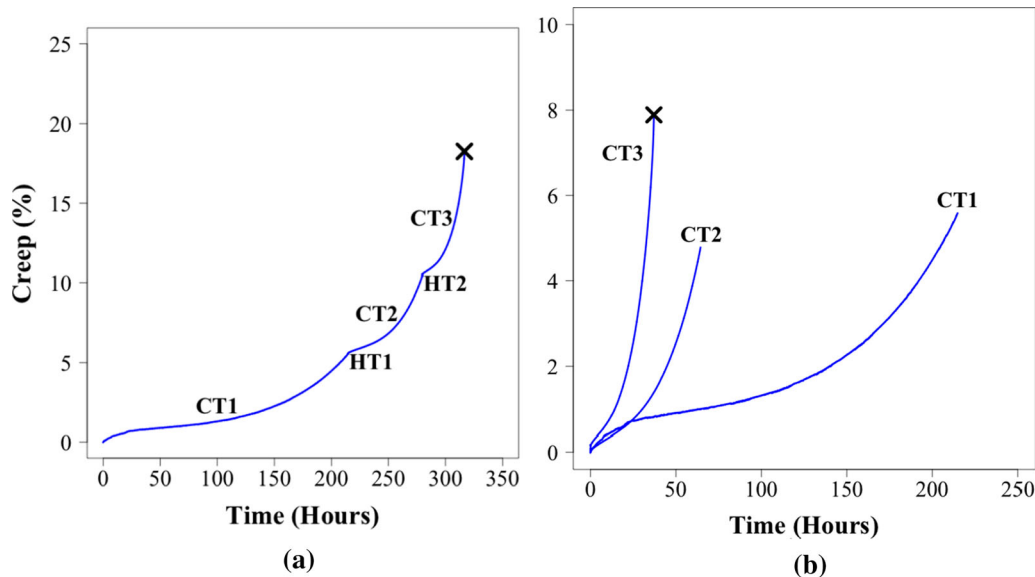


Fig. 8—(a) Multiple rejuvenation creep plot of N5-28-5 with a creep strain threshold of 5 pct strain. Each creep test and rejuvenation heat treatment are labeled. (b) Plotting each creep curve with the same reference point allows for direct comparison between tests.

**Table V. Summary of the Important Creep Parameters from the Multiple Rejuvenation Tests Performed on René N5(SX) Creep Specimens**

René N5(SX) Multiple Rejuvenation Tests			
	$\dot{\epsilon}_0$ ( $s^{-1}$ )	Creep Time (h)	Strain ( pct)
<b>2 pct Creep Strain Threshold</b>			
CT1	$4.72 \times 10^{-9}$	181.40	2.00
CT2	$1.69 \times 10^{-8}$	150.98	2.01
CT3	$1.86 \times 10^{-8}$	149.45	2.02
CT4	$1.72 \times 10^{-8}$	157.36	2.14
CT5	$1.58 \times 10^{-8}$	151.47	1.98
CT6	$1.75 \times 10^{-8}$	146.91	2.00
CT7	—	14.31	0.14
Totals		951.87	12.30
<b>3 pct Creep Strain Threshold</b>			
CT1	$7.22 \times 10^{-9}$	214.72	3.00
CT2	$1.36 \times 10^{-8}$	184.50	3.01
CT3	$1.42 \times 10^{-8}$	180.46	3.03
CT4	$1.47 \times 10^{-8}$	183.65	3.09
CT5	$1.39 \times 10^{-8}$	176.97	2.99
CT6	—	10.67	0.05
Totals		950.97	15.17
<b>5 pct Creep Strain Threshold</b>			
CT1	$1.58 \times 10^{-8}$	214.9	5.59
CT2	$6.81 \times 10^{-8}$	64.5	4.78
CT3	$1.32 \times 10^{-7}$	37.2	7.89
Totals		316.5	18.26

The creep test number (CT#) corresponds to the labeled creep curves in Figs. 8 and 9. The minimum creep rate,  $\dot{\epsilon}_0$ , creep time, and strain for each test are reported. CT3 for the 5 pct creep strain threshold test was tested to rupture due to unsuccessful rejuvenation. Rejuvenation heat treatments were only performed at a temperature of 28 °C below the  $\gamma'$  solvus.

reduced gage section of both tests N5-28-2 and N5-28-3 recrystallized with several dominant recrystallized grains being observed.

Resonant ultrasound spectroscopy revealed shifts in the frequencies in the resonant peaks, discussed in more detail in Section IV-D, indicating that detectable levels of recrystallization were present after the final rejuvenation heat treatment before failure for each creep specimen. This corresponds to HT6, HT5, and HT2 for the 2, 3, and 5 pct creep strain threshold tests, respectively. Recrystallization and the corresponding surface cracks caused rupture and prevented indefinite rejuvenation. Compared to an uninterrupted creep test, failure due to recrystallization did not involve significant void growth and is comparable to the failure of a polycrystalline specimen.

#### B. Influence of the Solution Temperature on Rejuvenation: René N5(SX)

With a critical strain threshold established, further multiple rejuvenation tests were performed using a 2 pct creep strain threshold, which is a conservative level of strain based on the interrupted testing. Additional solution temperatures of the  $\gamma'$  solvus and 56 °C below the  $\gamma'$  solvus were investigated during rejuvenation. This is in addition to the prior test N5-28-2, which used a 2 pct creep strain threshold and a solution temperature 28 °C below the  $\gamma'$  solvus, as shown in Figure 9. Figure 11 shows the results of N5-FS-2 and N5-56-2, with the important creep testing results being listed in Table VI.

A rejuvenation heat treatment at the  $\gamma'$  solvus, test N5-FS-2, was unable to completely recover the initial creep performance. However, it did provide the best rejuvenated creep performance when compared to lower solution temperatures. Similar to the 2 and 3 pct creep strain threshold tests performed with solutioning 28 °C below the  $\gamma'$  solvus, each subsequent creep test maintained a consistent minimum creep rate and time to the creep strain threshold. The overall creep rupture life was

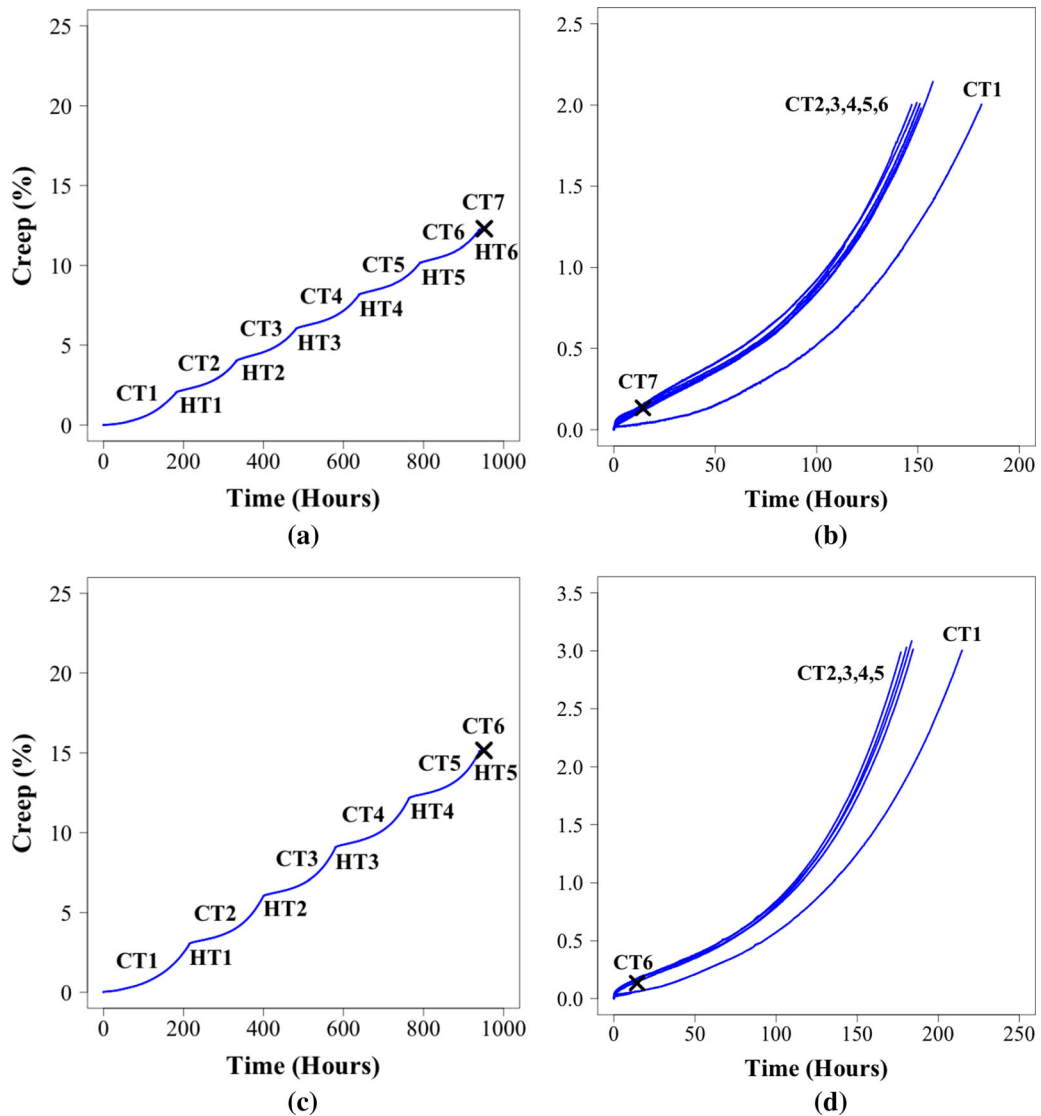


Fig. 9—Multiple rejuvenation ((a) and (c)) creep plots for René N5(SX) tests N5-28-2 and N5-28-3, with a creep strain threshold of 2 pct and 3 pct strains, respectively. Each creep test and rejuvenation heat treatment is labeled. Plotting each creep curve with the same reference point ((b) and (d)) allows for direct comparison between each test.

625 hours, a factor of 1.8 increase over the baseline creep test. Multiple rejuvenation at the  $\gamma'$  solvus resulted in the lowest observed creep rupture strain of 8 pct. A longer total creep rupture life of 812 hours was observed for N5-56-2, a factor of 2.4 increase over the baseline. The total rupture strain was 20.5 pct, a result of ten creep tests, and a corresponding nine rejuvenation heat treatments before failure. Due to the low solution temperature, the creep performance (minimum creep rate and time to creep strain threshold) degraded rapidly between the first and second test, comparable to N5-28-5. Property degradation continued during subsequent creep tests and did not stabilize. As mentioned previously, test N5-28-2, which had a creep strain threshold of 2 pct and a solution temperature of 28 °C below the  $\gamma'$  solvus, resulted in the longest total creep rupture life of the solution temperatures investigated and established consistent creep performance

(equivalent minimum creep rate and creep time) between CT2 through CT6.

EBSD of the specimens after failure showed that limited surface recrystallization was observed in the necked region after failure for test N5-56-2 while a majority of the reduced gage section recrystallized in tests N5-FS-2 and N5-28-2, as shown in Figures 10(a) and 12. Note that while the lowest solution temperature specimen did not rupture, due to significant necking, it was deemed to have failed. NDE indicated that recrystallization occurred during the last rejuvenation heat treatment (HT4) for N5-FS-2. For test N5-56-2, the volume of recrystallized material was not significant enough for RUS to detect, indicating that the NDE technique is only capable of detecting recrystallization after a critical volume fraction of recrystallized material has been reached, assuming a random orientation of recrystallized grains. In the next section, the multiple rejuvenation



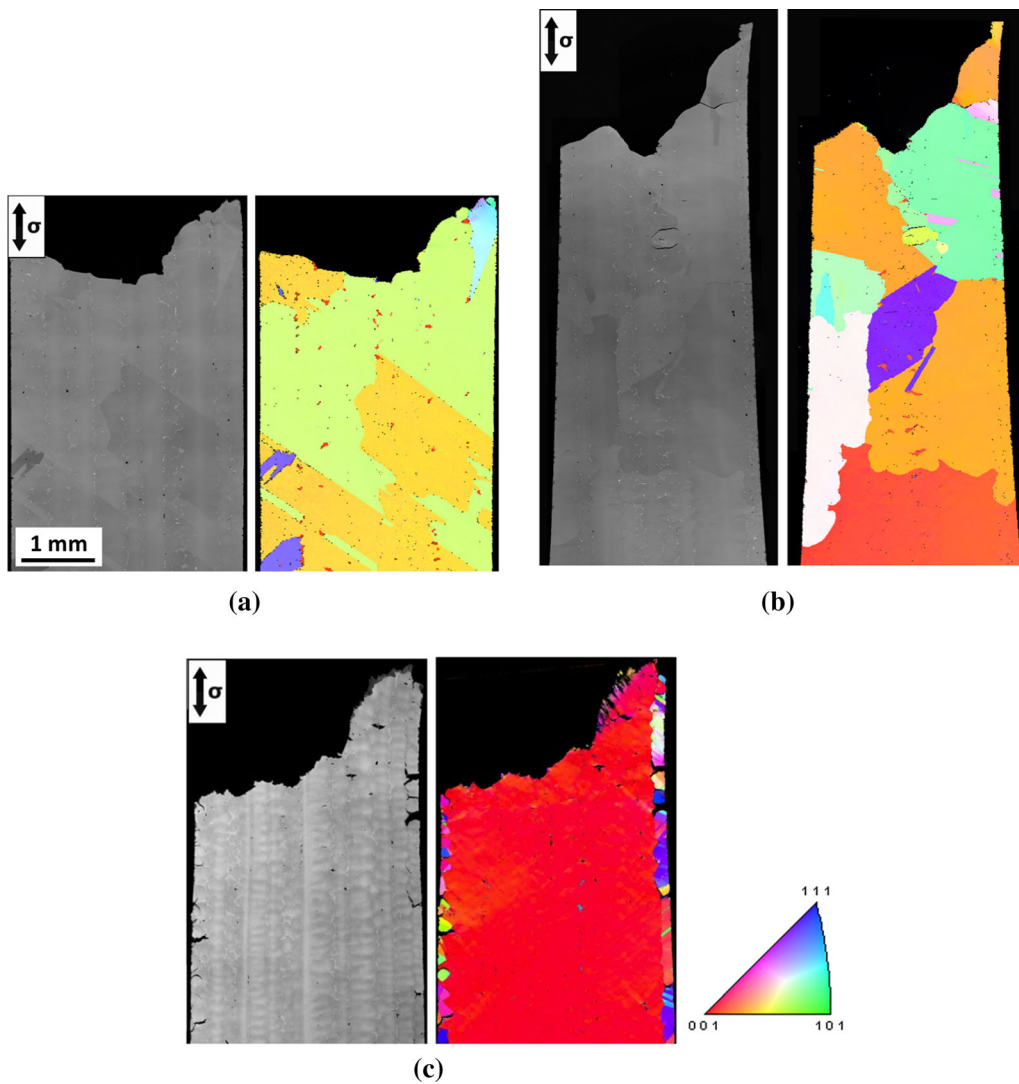


Fig. 10—Backscattered electron images and inverse pole figure maps with respect to the loading direction of René N5(SX) specimens with a strain threshold of (a) 2 pct, (b) 3 pct, and (c) 5 pct corresponding to tests N5-28-2, N5-28-3, and N5-28-5, respectively. The loading direction is indicated in the images and the scale is the same for each micrograph and EBSD scan.

testing results of GTD444(DS) specimens will be discussed and compared to the René N5(SX) results.

### C. Multiple Rejuvenation: Creep of GTD444(DS)

Rejuvenation heat treatments for GTD444(DS) were performed at a solution temperature 14 °C below the  $\gamma'$  solvus to recover the initial  $\gamma'$  morphology. The results of testing to 1, 2, and 3 pct creep strain thresholds are shown in Figure 13, and listed in Table VII. All GTD444(DS) specimens were crept at 982 °C/179 MPa. Test 444-14-1 was the most successful with a total creep rupture life and rupture strain of 1037 hours and 6.7 pct, respectively. The baseline creep performance of GTD444(DS) had a rupture life and rupture strain of 740 hours and 8.2 pct, respectively. At the solution temperatures and creep strain thresholds investigated, a stable minimum creep rate and creep behavior were not established by the rejuvenation heat treatment. Two tests were performed at a creep strain threshold of

2 pct to illustrate the variability in creep performance. Tests 444-14-2a and 444-14-2b had total rupture lives of 600 and 819 hours and rupture strains of 4.88 pct and 5.01 pct, respectively. Using a 3 pct creep strain threshold in test 444-14-3 resulted in an increased total rupture life compared to test 444-14-2a of 778 hours, 38 hours longer than the baseline.

NDE of the GTD444(DS) specimens detected recrystallization during tests 444-14-2a, 444-14-2b, and 444-14-3 after the final rejuvenation heat treatment, corresponding to HT2 for each test. Detectable levels of recrystallization were not present in test 444-14-1. EBSD scans and BSE images confirmed the presence of recrystallization in tests 444-14-2a, 444-14-2b, and 444-14-3, as shown in Figure 14. EBSD scans from test 444-14-2a also showed the presence of secondary dendrite arms from a neighboring primary dendrite, as shown in Figure 14(b). The secondary dendrite arms resulted in the presence of high-angle surface boundaries (> 25°) oriented transverse to the loading direction.

**Table VI. Summary of the Important Creep Parameters for Multiple Rejuvenation Tests Performed on René N5(SX) Creep Specimens with Two Different Rejuvenation Solution Temperatures of 56 °C Below and at the  $\gamma'$  Solvus**

René N5(SX) Multiple Rejuvenation Tests			
	$\dot{\epsilon}_0$ (s <sup>-1</sup> )	Creep Time (h)	Strain (Pct)
Rejuvenation at the $\gamma'$ Solvus			
CT1	$7.78 \times 10^{-9}$	161.63	2.00
CT2	$1.42 \times 10^{-8}$	152.13	2.00
CT3	$1.39 \times 10^{-8}$	152.40	1.96
CT4	$1.42 \times 10^{-8}$	156.69	2.00
CT5	—	2.34	0.04
Totals		625.20	8.00
	$\dot{\epsilon}_0$ (s <sup>-1</sup> )	Creep Time (h)	Strain (Pct)
Rejuvenation at 56 °C below the $\gamma'$ Solvus			
CT1	$9.17 \times 10^{-9}$	173.13	1.99
CT2	$2.39 \times 10^{-8}$	115.55	2.00
CT3	$3.50 \times 10^{-8}$	89.49	2.02
CT4	$4.31 \times 10^{-8}$	75.75	2.01
CT5	$5.17 \times 10^{-8}$	71.70	2.14
CT6	$5.36 \times 10^{-8}$	66.33	2.01
CT7	$5.19 \times 10^{-8}$	68.39	2.00
CT8	$6.47 \times 10^{-8}$	58.14	2.14
CT9	$7.28 \times 10^{-8}$	51.20	2.13
CT10	$7.94 \times 10^{-8}$	42.52	2.03
Totals		812.19	20.47

The creep test number (CT#) corresponds to the labeled creep curves in Fig. 11. The minimum creep rate ( $\dot{\epsilon}_0$ ), creep time, and strain for each test are reported. A 2 pct creep strain threshold was used for both tests.

### 1. Multiple Rejuvenation: Creep of a $\beta$ -NiAl-Coated René N5(SX) Specimen

In order to determine the influence of coatings on rejuvenation, a  $\beta$ -NiAl-coated René N5(SX) specimen was tested. The presence of a coating may aid in the rejuvenation of creep properties by inhibiting surface-nucleated recrystallization that progresses to complete recrystallization as demonstrated by Bürgel *et al.*<sup>[26]</sup> In addition,  $\beta$ -NiAl-coated René N5(SX) creep specimens should not contain a  $\gamma'$  depletion zone due to the reservoir of aluminum provided by the coating and will instead have an interdiffusion zone (IDZ) between the coating and superalloy substrate. An aluminate coating is commonly used to promote the formation of a slow-growing and adherent  $\alpha$ -Al<sub>2</sub>O<sub>3</sub> oxide scale, which serves as a barrier to oxygen diffusion and provides compatibility with a ceramic top coat. Coatings were applied by using an aluminizing process that involved exposing René N5(SX) specimens to a high Al activity environment. This was followed by a diffusion heat treatment to promote the inward diffusion of Al and outward diffusion of Ni creating the IDZ. The IDZ has been shown to be rich in slow diffusing elements such as Re, Ta, and W.<sup>[27]</sup>

A baseline creep test of  $\beta$ -NiAl-coated René N5(SX) at 982 °C/206 MPa resulted in a total rupture life and rupture strain of 201 hours and 34 pct, respectively. The

rupture life was reduced by 144 hours when compared to the baseline-uncoated René N5(SX) creep performance at the same testing conditions. The decrease in life was a result of several factors, including the loss of the  $\gamma/\gamma'$  microstructure near the coating–substrate interface due to interdiffusion. Creep testing from literature indicates that the creep rate of [001] oriented single crystals of  $\beta$ -NiAl is approximately 8 orders of magnitude higher than  $\gamma/\gamma'$  containing superalloys.<sup>[28]</sup> Degradation of the coating also occurs during creep testing and rejuvenation heat treatments, influencing mechanical performance. Diffusion of Ni and Al during high-temperature exposure and Al depletion due to oxidation leads to the formation of a two phase  $\beta$  and  $\gamma'$  coating. The Ta-rich  $\gamma'$  grains that develop are susceptible to catastrophic oxidation.<sup>[29]</sup> A topologically closed packed (TCP) phase,  $\sigma$ , rich in Re, W, and Cr, also forms as a result of interdiffusion due to a decreased Ni activity in the  $\gamma$  phase.<sup>[29,30]</sup> At high temperatures (> 850 °C), TCP phases decrease creep rupture life primarily due to the depletion of solid solution strengtheners from the matrix phase.<sup>[14,27,31]</sup> Micrographs collected after rupture of the baseline and rejuvenated  $\beta$ -NiAl-coated René N5(SX) specimens showed the presence of the  $\gamma'$  phase in the coating, precipitation of TCP phases, and creep cavities, as shown in Figure 15.

Multiple rejuvenation testing of a  $\beta$ -NiAl-coated René N5(SX) specimen resulted in a total rupture life of 541 hours, an increase of a factor of 2.7 compared to the baseline, but had a reduced creep rupture ductility of 13.6 pct. The results for each creep test are listed in Table VIII and shown graphically in Figure 16. Recrystallization was not detected by NDE or post-rupture metallographic examination, supporting the theory that recrystallization in the uncoated René N5(SX) specimens was initiated at or near the surface of the specimen.

### D. Experimental RUS Results from Multiple Rejuvenation Testing

Based on the expected behavior of recrystallization on resonance and to simplify the analysis, three reliably measured resonant bending modes were selected and tracked during multiple rejuvenation testing. Scans were collected before and after each creep test and rejuvenation heat treatment. The tracked modes correspond to FE-model-informed mode numbers 9–10, 11–12, and 13–14. These were selected out of the 50 total modes for the frequency scan range of 1–200 kHz. Only the  $f_R$  are monitored with a focus on the evolution of mode-specific changes in  $f_R$  ( $\Delta f_R$ ), defined as follows:

$$\Delta f_R = \frac{f_R^{\text{new condition}} - f_R^{\text{previous condition}}}{f_R^{\text{previous condition}}} * 100\text{pct}. \quad [4]$$

The influence of creep deformation on the  $\Delta f_R$  is evident by constructing a box plot of all experimentally measured points from the three sets of bending mode pairs for both GTD444(DS) and René N5(SX), as shown in Figure 17(a). A linear regression fit to the data indicates

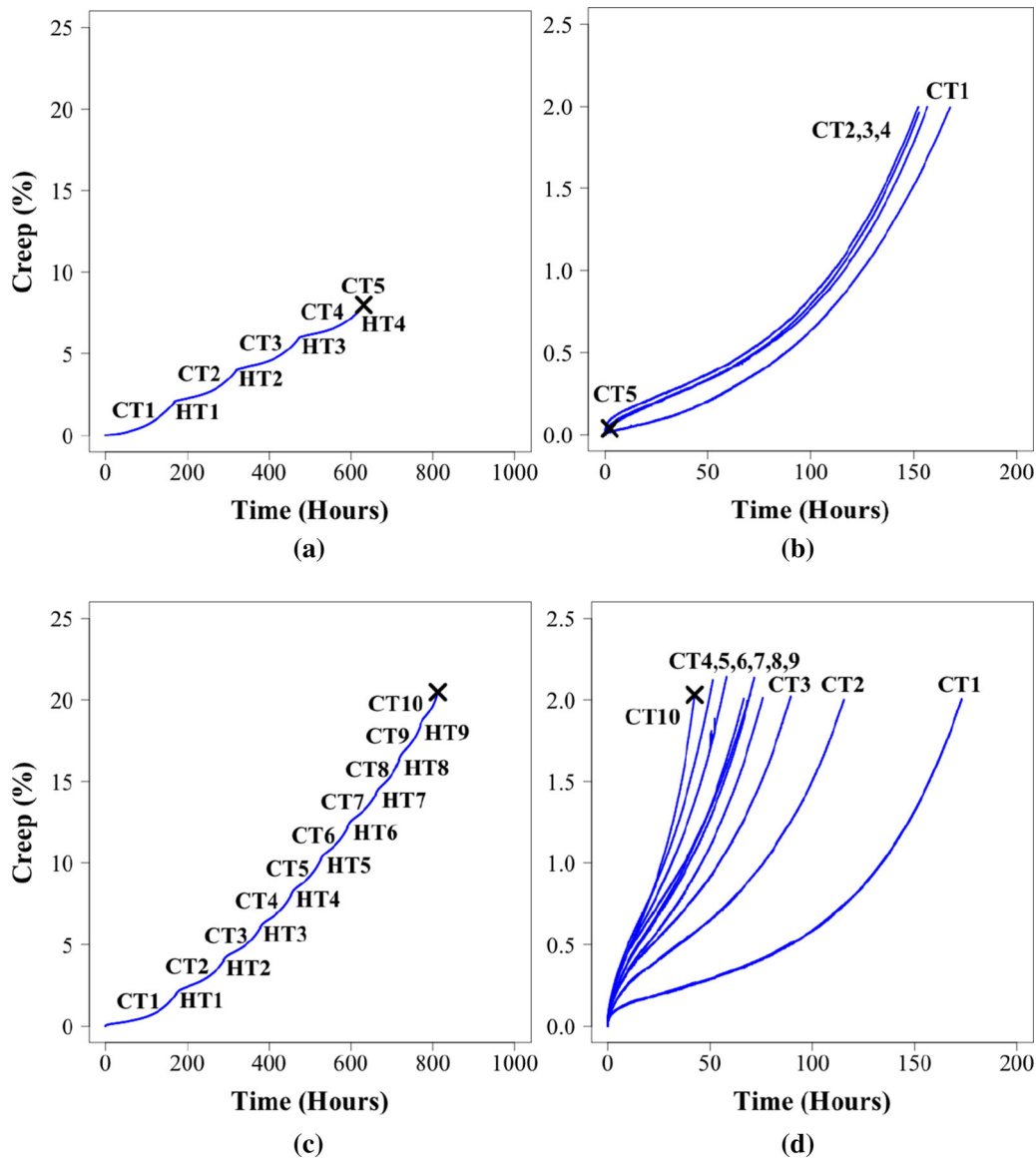


Fig. 11—Multiple rejuvenation ((a) and (c)) creep plots for René N5(SX) with solution temperatures at the  $\gamma'$  solvus and  $56^\circ\text{C}$  below the  $\gamma'$  solvus, respectively (corresponding to tests N5-FS-2 and N5-56-2, respectively). Each creep test and rejuvenation heat treatment are labeled. Each creep curve is plotted with the same reference point ((b) and (d)) for direct comparison between tests.

that up to 5 pct creep strain that there is an inverse linear relationship between  $\Delta f_R$  and creep strain. This is a result of specimen elongation and the corresponding increase in the wavelength and decrease in resonance frequency due to the inverse relationship between wavelength and resonance frequency. The bending mode pairs were analyzed collectively because they each supported the inverse linear relationship with  $r^2$  values of between 0.6 and 0.8. The dominant influence of specimen elongation on the  $\Delta f_R$  makes it difficult to use RUS to determine the presence of cracks and cavities non-destructively at low creep strains, because they would also result in a decrease in the resonance frequency by reducing the specimen's effective elastic modulus.<sup>[32]</sup>

However, RUS was successful in non-destructively detecting the presence of recrystallization. Box plots, showing the results from all René N5(SX) and GTD444(DS) multiple rejuvenation specimens (Figures 17(b) and (c), respectively), consistently show a statistically significant difference in the  $\Delta f_R$  after the final rejuvenation heat treatment before failure, as discussed previously. It was later confirmed via metallographic examination that recrystallization was present in these specimens. The average  $\Delta f_R$  from the rejuvenation heat treatment that caused significant recrystallization was  $4.31 \pm 3.19$  pct and  $1.36 \pm 1.31$  pct for René N5(SX) and GTD444(DS), respectively. René N5(SX) showed a more significant  $\Delta f_R$  when compared to GTD444(DS) due to the inherent differences in grain



structure between a SX and a DS material. A DS creep specimen will, on average, have several grains through thickness and contain high-angle twist boundaries, resulting in a higher baseline elastic modulus. Thus, recrystallization will have a less significant influence on the elastic properties when compared to a well-aligned single crystal. Furthermore, recrystallization in a single-crystal specimen was observed to consume a majority of the reduced gage section. The same could not be said for recrystallization in GTD444(DS), which was more limited. One René N5(SX) multiple rejuvenation specimen that was interrupted before complete rupture did not display a statistically significant  $\Delta f_R$  but limited surface recrystallization was present. This result indicates that the RUS technique is detecting recrystallization only after a critical volume fraction of recrystallized material has been reached, assuming a random orientation of recrystallized nuclei. Thus, RUS did not detect the onset of recrystallization but rather the onset of a statistically significant change in the elastic properties resulting from catastrophic levels of recrystallization. The presence of detectable levels of recrystallization always resulted in abrupt specimen rupture during multiple rejuvenation creep testing.

The typical  $\Delta f_R$  from a rejuvenation heat treatment was low and negative at approximately  $-0.226 \pm 0.456$  pct and  $0.040 \pm 0.31$  pct for René N5(SX) and GTD444(DS), respectively. The negative  $\Delta f_R$  was believed to be a result of the reduction of mixed oxides during the rejuvenation heat treatment, which was performed in a 5 pct  $H_2/Ar$  environment, causing a mass change. The baseline heat treatment, displayed at HT0 in Figures 17(b) and (c), showed the greatest scatter in  $\Delta f_R$  between the three pairs of bending modes and from specimen to specimen. This may be a result of the relaxation of residual stress imparted on the specimens during machining.

In summary, there is strong evidence that RUS can be used to detect recrystallization; however, detecting other forms of damage will be difficult at the creep strains of interest due to concurrent small changes in geometry during mechanical testing.

#### E. Multiple Rejuvenation: Fatigue of René N5(SX)

SPLCF testing was conducted on bare René N5(SX) at a temperature of 982 °C in air with a strain range of 0.6 pct and  $R = -\infty$  ( $A = -1.0$ ). Refer to Section II–B for additional information on the SPLCF testing procedure and experimental setup. Rejuvenation heat treatments employed a solution temperature of 28 °C below the  $\gamma'$  solvus. Multiple rejuvenation of René N5(SX) led to a factor of 2 increase in fatigue life compared to the baseline with no sign of impending failure, as shown in Figure 18. The increase in fatigue life only depended on the removal of previously formed fatigue cracks and not on the application of a rejuvenation heat treatment, indicating that significant recovery of the dislocation substructure is not necessary to extend SPLCF life. Subsequent crack formation and growth do not appear to be influenced by the preexisting dislocation substructure, but rather near-surface plasticity and defects such as surface undulations and oxide cracks. This is in sharp contrast to rejuvenation of creep specimens where recovery of dislocation substructure to a near-virgin state is necessary to maintain creep properties.<sup>[33]</sup>

Rejuvenation was limited by the amount of material remaining in the gage section of the fatigue specimens. Approximately 400–600  $\mu m$  of material was polished away after each fatigue test to remove all fatigue cracks, significantly greater than the maximum crack length of 91  $\mu m$  observed *via* optical microscopy on 2D cross sections.<sup>[34]</sup> This illustrates the importance of 3D microstructural characterization and the development

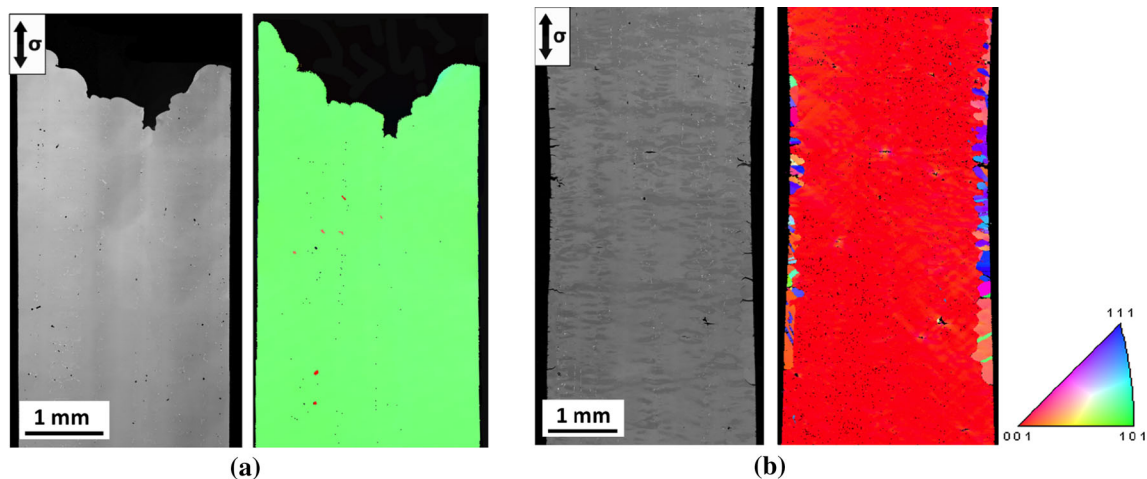


Fig. 12—Backscattered electron images and inverse pole figure maps with respect to the loading direction. Images are from multiple rejuvenation tests of René N5(SX) tests N5-FS-2 and N5-56-2, with a strain threshold of 2 pct and solution temperatures during rejuvenation (a) at the  $\gamma'$  solvus and (b) 56 °C below the  $\gamma'$  solvus, respectively. The loading direction is indicated on both images. The scale is the same for each micrograph and EBSD scan.

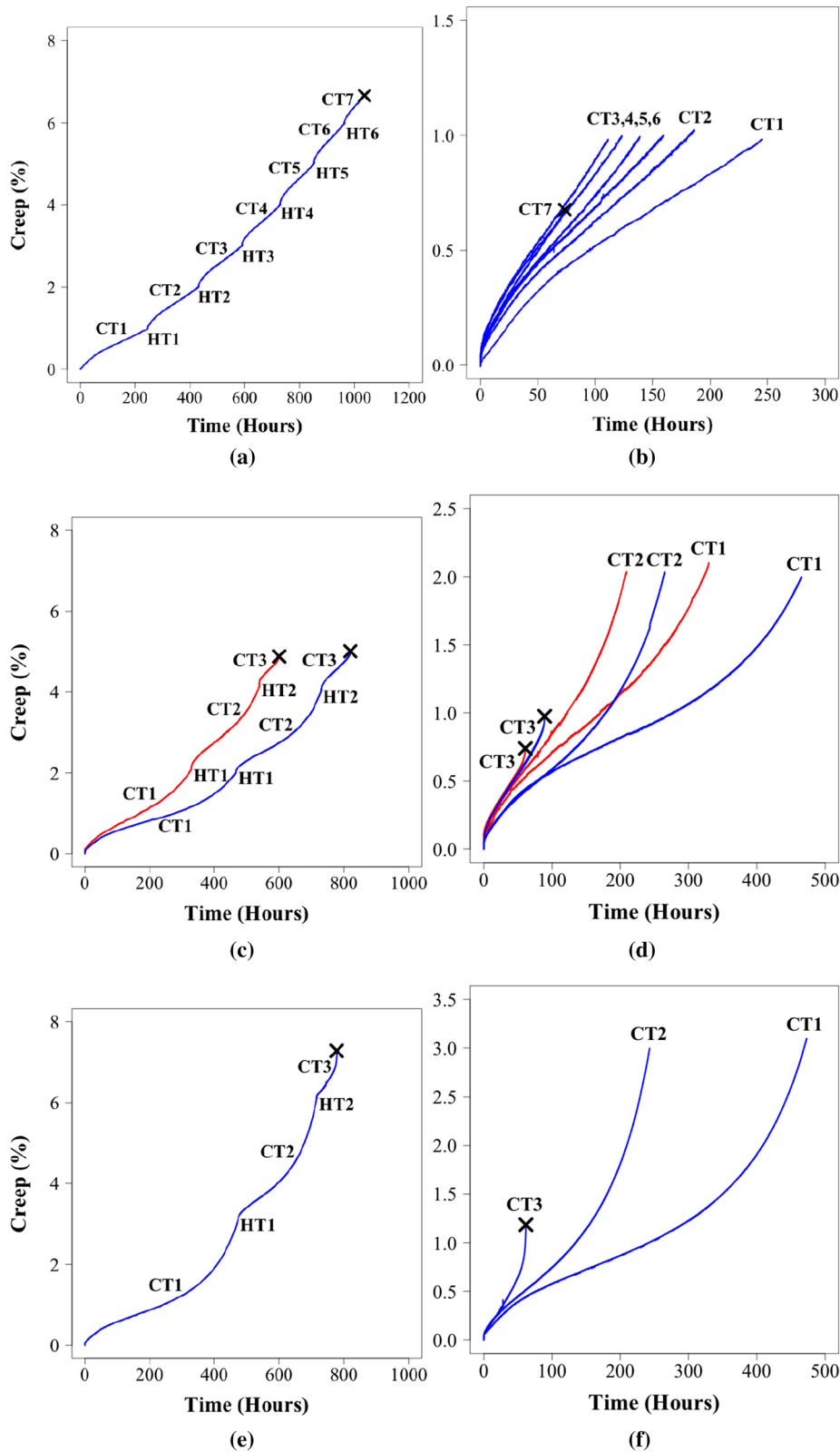


Fig. 13—Multiple rejuvination ((a), (c), and (e)) creep plots for GTD444(DS) tests 444-14-1, 444-14-2a, 444-14-2b, and 444-14-3, which were solutioned 14 °C below the  $\gamma'$  solvus and tested to creep strain thresholds of 1 pct, 2 pct, and 3 pct, respectively. Each creep test and rejuvination heat treatment are labeled. Plotting each creep curve with the same reference point ((b), (d), and (f)) allows for direct comparison between each test. The red and blue creep curves (color version available online) for the 2 pct creep strain threshold tests correspond to 444-14-2a and 444-14-2b, respectively.

of NDE techniques to more accurately determine crack length.

## V. DISCUSSION OF THE RESULTS OF MULTIPLE REJUVENATION TESTING

As a result of multiple rejuvenation testing, the total creep rupture life of René N5(SX) tested at 982 °C and 206 MPa was extended by a factor of 2.8 over the baseline rupture life. To produce this increase in rupture life, creep strain thresholds of both 2 and 3 pct were used along with solutioning at 28 °C below the  $\gamma'$  solvus temperature for 2 hour and aging at 1079 °C for 4 hour. These rejuvenation conditions resulted in the maximum observed increase in total creep rupture life. In addition to the extension in creep life, the creep curve shape was recovered and the time to the creep strain threshold was maintained above 80 pct of the initial creep test. Based on the multiple rejuvenation tests performed, an appropriate criterion for successful rejuvenation of creep properties was the recovery of 80 pct of the initial time to the creep strain threshold, with the baseline determined by the first creep test performed during a multiple rejuvenation test. This criterion was applied to both GTD444(DS) and René N5(SX).

Successful rejuvenation required a creep strain threshold below 5 pct. The failure of a rejuvenation heat treatment to recover macroscopic plastic strain near 5 pct is most likely a combination of an increased dislocation density and enhanced plasticity near stress concentrators such as carbides and pores. As expected, the solution temperature used during the rejuvenation heat treatment had an impact on the amount of recovery and recrystallization. Solutioning at the  $\gamma'$  solvus for René N5(SX) resulted in the greatest recovery of the initial creep performance but only increased the total creep rupture life by a factor of 1.8 due to the nucleation of recrystallized grains. As the solution temperature is decreased, the volume fraction of unsolutioned  $\gamma'$  increases, helping to suppress the growth of recrystallization nuclei. A clear tradeoff exists between recovery and suppressing recrystallization that results in an optimal solution temperature of 28 °C below the  $\gamma'$  solvus temperature for René N5(SX) at a creep strain threshold of 2 pct.

At lower solution temperatures, the volume fraction of unsolutioned  $\gamma'$  increases, helping to suppress the growth of recrystallization nuclei. The unsolutioned  $\gamma'$  is primarily located in the interdendritic region where the local  $\gamma'$  solvus is higher due to solidification-induced segregation of  $\gamma'$  forming elements Al, Nb, Ta, and

**Table VII. Summary of the Important Creep Parameters from the Multiple Rejuvenation Tests Performed on GTD444(DS) Creep Specimens**

GTD444(DS) Multiple Rejuvenation Tests			
	$\dot{\epsilon}_0$ ( $s^{-1}$ )	Creep Time (h)	Strain (Pct)
1 pct Creep Strain Threshold			
CT1	$8.61 \times 10^{-9}$	241.11	0.98
CT2	$1.19 \times 10^{-8}$	185.90	1.02
CT3	$1.33 \times 10^{-8}$	159.44	1.00
CT4	$1.47 \times 10^{-8}$	138.93	1.00
CT5	$1.72 \times 10^{-8}$	123.22	1.00
CT6	$1.86 \times 10^{-8}$	111.14	0.98
CT7	$2.00 \times 10^{-8}$	73.50	0.68
	Totals	1037.24	6.66
2 pct Creep Strain Threshold (444-14-2a)			
CT1	$1.11 \times 10^{-9}$	329.74	2.10
CT2	$1.75 \times 10^{-8}$	209.10	2.04
CT3	$2.31 \times 10^{-8}$	60.95	0.74
	Totals	599.79	4.88
2 pct Creep Strain Threshold (444-14-2b)			
CT1	$6.67 \times 10^{-9}$	465.00	2.00
CT2	$1.11 \times 10^{-8}$	265.15	2.04
CT3	$1.97 \times 10^{-8}$	89.17	0.98
	Totals	819.32	5.01
3 pct Creep Strain Threshold			
CT1	$7.78 \times 10^{-9}$	472.95	3.10
CT2	$1.58 \times 10^{-8}$	242.91	3.00
CT3	$2.50 \times 10^{-8}$	61.73	1.19
	Totals	777.59	7.28

The creep test number (CT#) corresponds to the labeled creep curves in Figs. 13. The minimum creep rate ( $\dot{\epsilon}_0$ ), creep time, and strain for each test are reported. Rejuvenation heat treatments were performed 14 °C below the  $\gamma'$  solvus.



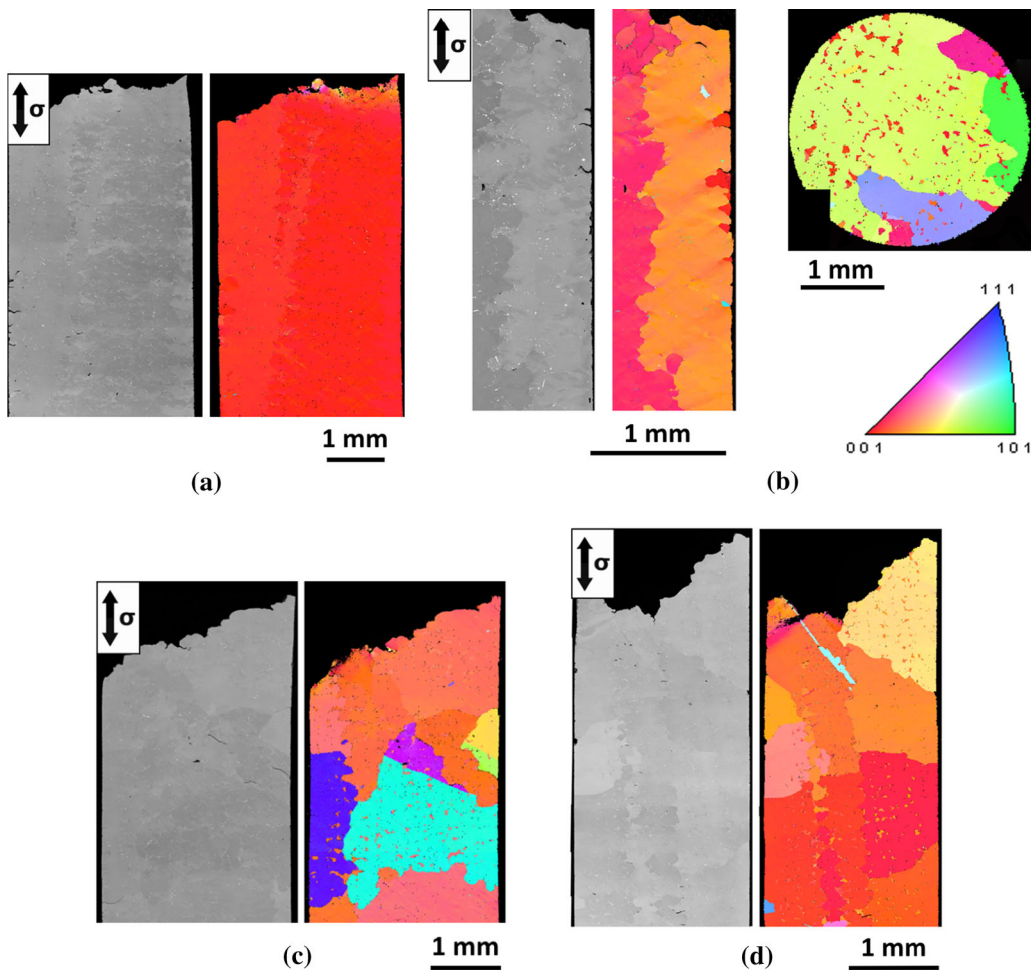


Fig. 14—Backscattered electron images and inverse pole figure maps with respect to the loading direction. Images correspond to multiple rejuvenation tests 444-14-1, 444-14-2a, 444-14-2b, and 444-14-3, with strain thresholds of (a) 1 pct, (b), (c) 2 pct, and (d) 3 pct, respectively. A transverse section of 444-14-2a was required to detect the recrystallization. The solution temperature during rejuvenation was 14 °C below the  $\gamma'$  solvus for all tests.

Ti.<sup>[14]</sup> The presence of unsolved  $\gamma'$  is expected to degrade creep performance by an increase in  $\gamma$  channel width and corresponding decrease of the Orowan stress due to precipitate coarsening during heat treatment.<sup>[35]</sup> The retention of misfit dislocation networks in unsolved areas may also increase creep rates when compared to virgin material by serving as dislocation sources.<sup>[36]</sup> Nevertheless, the debit associated with the presence of the unsolved  $\gamma'$  is compensated by its role in suppressing recrystallization.

#### A. Suppressing Recrystallization During Rejuvenation

Recovery is a precursor to the nucleation of recrystallized grains, thus, avoiding recrystallization during rejuvenation presents a significant challenge. However, experimental observations indicate that recrystallization

has been avoided up to 5 pct creep strain for solution heat treatments below the  $\gamma'$  solvus temperature. This indicates that the nucleation and growth of recrystallized grains in DS and SX Ni-base superalloys may be inherently difficult due to the dislocation substructure formed under the influence of a large volume fraction of misfitting  $\gamma'$  precipitates and the pinning effect of the  $\gamma'$  precipitates.

Investigations of the annealing/solution temperature limits and strain limits of recrystallization have been performed in the literature by Cox *et al.*, and Bürgel *et al.*<sup>[26,37]</sup> Cox *et al.* performed tensile tests at 950 °C and 1025 °C with a strain rate of  $4 \times 10^{-4} \text{ s}^{-1}$  to 4 pct plastic strain and then conducted annealing treatments at various temperatures for 6 hours. Recrystallization was not observed following annealing at 1260 °C (55 °C below the  $\gamma'$  solvus) and below for specimens deformed

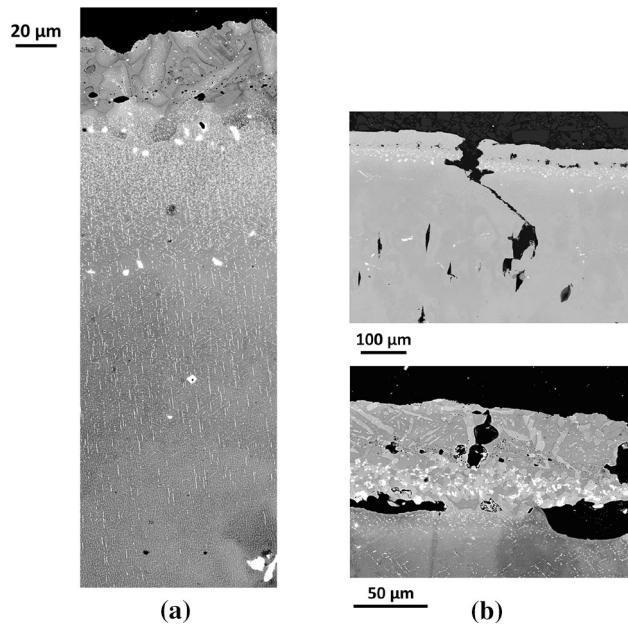


Fig. 15—(a) Micrographs of the baseline  $\beta$ -NiAl-coated René N5(SX) creep specimen tested to failure. (b) Additional low-magnification (top) and high-magnification (bottom) images of the multiple rejuvenation  $\beta$ -NiAl-coated René N5(SX) creep specimen after failure.

**Table VIII. Table Listing the Important Creep Parameters from a  $\beta$ -NiAl-Coated René N5(SX) Multiple Rejuvenation Test**

$\beta$ -NiAl-Coated René N5(SX) Multiple Rejuvenation Tests			
	$\dot{\epsilon}_0$ ( $s^{-1}$ )	Creep Time (h)	Strain (Pct)
CT1	$1.44 \times 10^{-8}$	106.38	1.994
CT2	$2.58 \times 10^{-8}$	86.42	2.032
CT3	$3.19 \times 10^{-8}$	81.79	2.052
CT4	$2.81 \times 10^{-9}$	78.47	2.034
CT5	$3.06 \times 10^{-8}$	74.99	2.000
CT6	$3.25 \times 10^{-8}$	76.23	1.994
CT7	$3.97 \times 10^{-9}$	36.74	1.523
Totals		541.02	13.63

The creep test number (CT#) corresponds to the labeled creep curves in Fig. 16. The minimum creep rate ( $\dot{\epsilon}_0$ ), creep time, and strain for each test are reported. Rejuvenation heat treatments were performed 28 °C below the  $\gamma'$  solvus and with a creep strain threshold of 2 pct.

at 950 °C, while recrystallization was observed at all annealing temperatures for specimens deformed at 1025 °C. Bürgel *et al.* used room-temperature axial compression tests to induce plastic strain and determined, for a variety of Ni-base superalloys that solutioning above the  $\gamma'$  solvus after at least 1 pct strain caused rapid recrystallization.<sup>[26]</sup> Grain nucleation occurred at the surface and, at annealing temperatures below the  $\gamma'$  solvus, the grain boundary motion was hindered by interdendritic  $\gamma'$  precipitates. Prior studies

are in good agreement with the coupon heat treatment results reported herein, specifically, the suppression of recrystallization at solution temperatures below the  $\gamma'$  solvus at strains up to 4–5 pct.

Rejuvenation of a coated specimen was able to extend creep life and demonstrated a method to suppress recrystallization-induced failure. However, degradation of the coating and precipitation of TCP phases, a result of interdiffusion between the coating and superalloy substrate, had a similar effect on the creep performance as the introduction of transverse grain boundaries. While not as catastrophic as recrystallization, where failure occurred during the subsequent creep test, coating degradation was a contributing factor in the decrease in creep performance after each rejuvenation heat treatment.

### B. Rejuvenation of Directionally Solidified vs. Single-Crystal Material

GTD444(DS), while less expensive and easier to produce than René N5(SX), has a more complex microstructure. Depending on where the creep specimen is machined from the plate of material, there can be a varying number of grains through the specimen thickness, leading to variability in creep properties. The volume fraction of unsolutioned phases was also higher in GTD444(DS) when compared to René N5(SX), as shown in Figure 2. The microstructure of GTD444(DS) contains additional damage initiation sites (carbides, eutectic pools, and grain boundaries) when compared to René N5(SX); these sites prevent successful recovery of creep properties and make GTD444(DS) less amenable to rejuvenation. Specifically, rejuvenation of GTD444(DS) was only able to extend the total creep life over the baseline by a factor of 1.4. In addition, a stable minimum creep rate and consistent creep behavior were not established during any test, which indicate that even at the lowest creep strain threshold of 1 pct, unrecoverable damage was present. The presence of unrecoverable damage was most likely a result of transverse high-angle grain boundaries. While ideally the high-angle boundaries of DS alloys should be oriented parallel to the loading direction, EBSD scans shown in Figure 14 indicate that due to the tortuosity of the grain boundaries, portions of the grain boundary area are oriented perpendicular to the loading direction. The low creep rupture ductility of the GTD444(DS) specimens supports this conclusion.

### C. Rejuvenation of Fatigue Damage

Damage from SPLCF testing was also successfully rejuvenated by removing surface cracks via small-scale material removal (polishing). While removing 400–600  $\mu$ m of material was achievable on a lab scale, implementation on a production scale will be challenging. In addition, the total number of rejuvenation cycles will be limited by the blade wall thickness instead of specimen

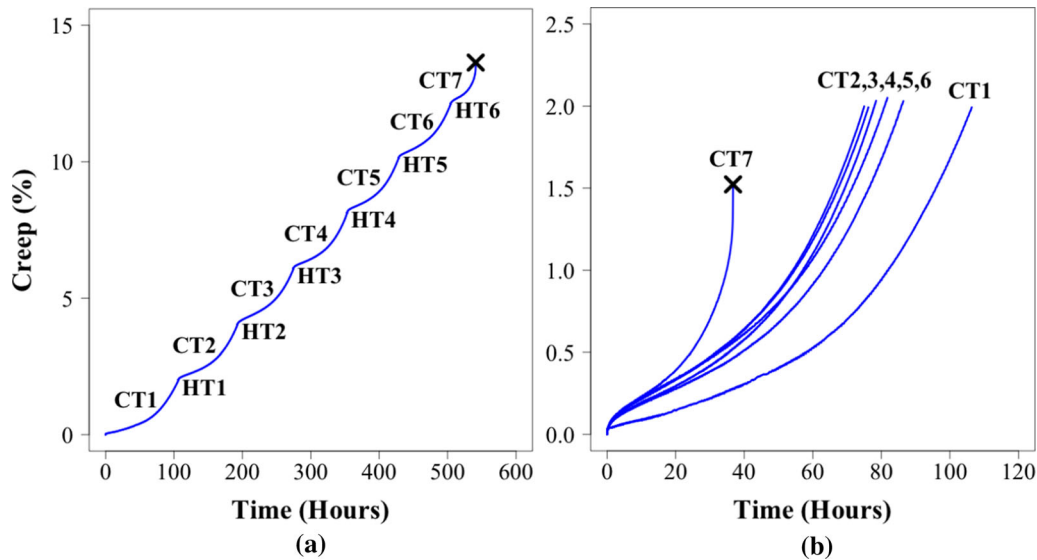


Fig. 16—(a) Creep curves from multiple rejuvenation testing of  $\beta$ -NiAl-coated René N5(SX) test N5-28-2-CT. (b) The creep curves are also plotted using the same reference point for direct comparison.

thickness. A better approach would be to use a high strength coating to suppress oxidation-induced surface crack growth, preventing the surface crack growth from transitioning into the substrate before the first rejuvenation cycle. Recoating could then be used to remove the SPLCF cracks.

## VI. CONSTRUCTION OF A REJUVENATION MAP

A René N5(SX) rejuvenation map was created as a convenient way to visualize the experimental results of multiple rejuvenation creep testing, Figure 19. Only creep tests with at least 80 pct recovery of the initial time to the creep strain threshold were considered successful. This criterion captured both early failure due to recrystallization and incomplete recovery. This successful rejuvenation criterion may not be appropriate for all situations and should be chosen on a case-by-case basis depending on the material and mechanical properties of interest. The area shaded red in Figure 19 (color version available online) indicates the region of total creep strain and number of rejuvenation cycles (note: a cycle included one creep test and one rejuvenation heat

treatment) where unsuccessful rejuvenation is expected to occur. Conversely, successful rejuvenation was further subdivided based on the solution temperature used during the rejuvenation heat treatment, with the green-shaded region being at the  $\gamma'$  solvus and blue region at 28 °C below the  $\gamma'$  solvus. The multiple rejuvenation tests used to generate this map included N5-FS-2, N5-28-2, N5-28-3, N5-28-5, and a 1 pct creep strain threshold multiple rejuvenation test that was not discussed previously because the test failed prematurely as a result of experimental error. The rejuvenation cycle when recrystallization occurred for each test has also been indicated on the map. More tests are required to produce an accurate map and as a result, the current map was conservatively constructed especially at a low total creep strain and a high number of rejuvenation cycles. The regions of uncertainty in the map are roughly outlined by the purple shading.

The general trends of the rejuvenation map are consistent with experimental results, namely that the creep strain threshold before rejuvenation should be below 5 pct and that solution heat treatment should be performed near 28 °C below the  $\gamma'$  solvus. When comparing the data from multiple rejuvenation tests N5-28-2 and N5-28-3, which had similar total rupture

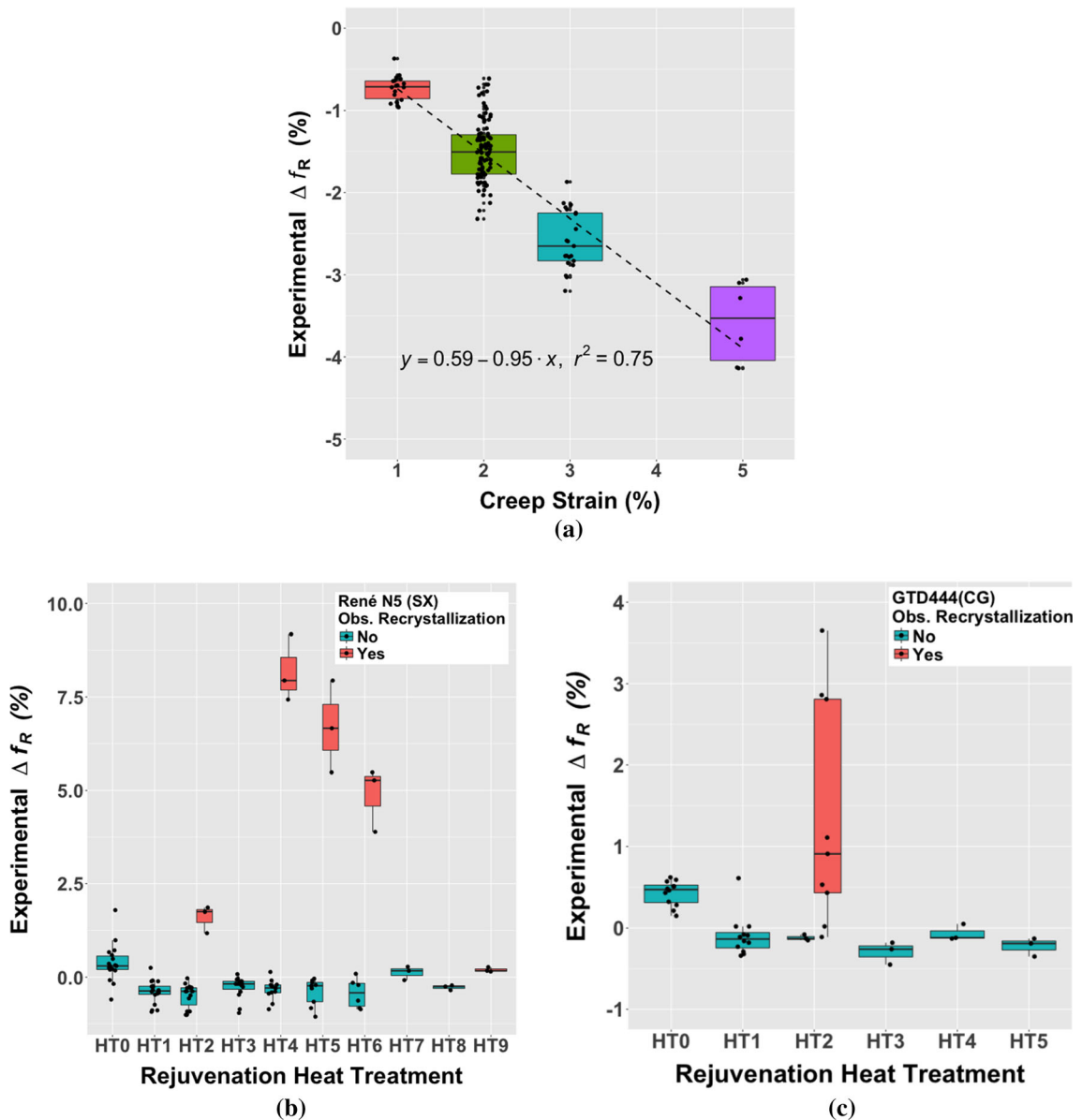


Fig. 17—Box plots showing the experimentally measured  $\Delta f_R$  due to (a) creep deformation and rejuvenation heat treatments of all multiple rejuvenation (b) René N5(SX) and (c) GTD444(DS) specimens. The box plots show a rectangle that spans the interquartile range. A black horizontal line inside the rectangle shows the median, and each measurement is plotted showing the minimum and maximum values. Each heat treatment is labeled with the baseline corresponding to HT0.

lives, N5-28-3 would be preferred due to fewer total rejuvenation cycles. It has been shown that the mechanisms preventing successful rejuvenation primarily depend on the extent of high-temperature exposure and the accumulation of strain. These factors result in the nucleation of recrystallized grains through the formation and growth of subgrains, which occurs at

stress concentrations near the surface where there is a reduced grain growth barrier due to the oxidation-induced depletion of  $\gamma'$  precipitates. Even without recrystallization, a critical accumulation of strain prior to rejuvenation prevents sufficient recovery of the initial creep properties.



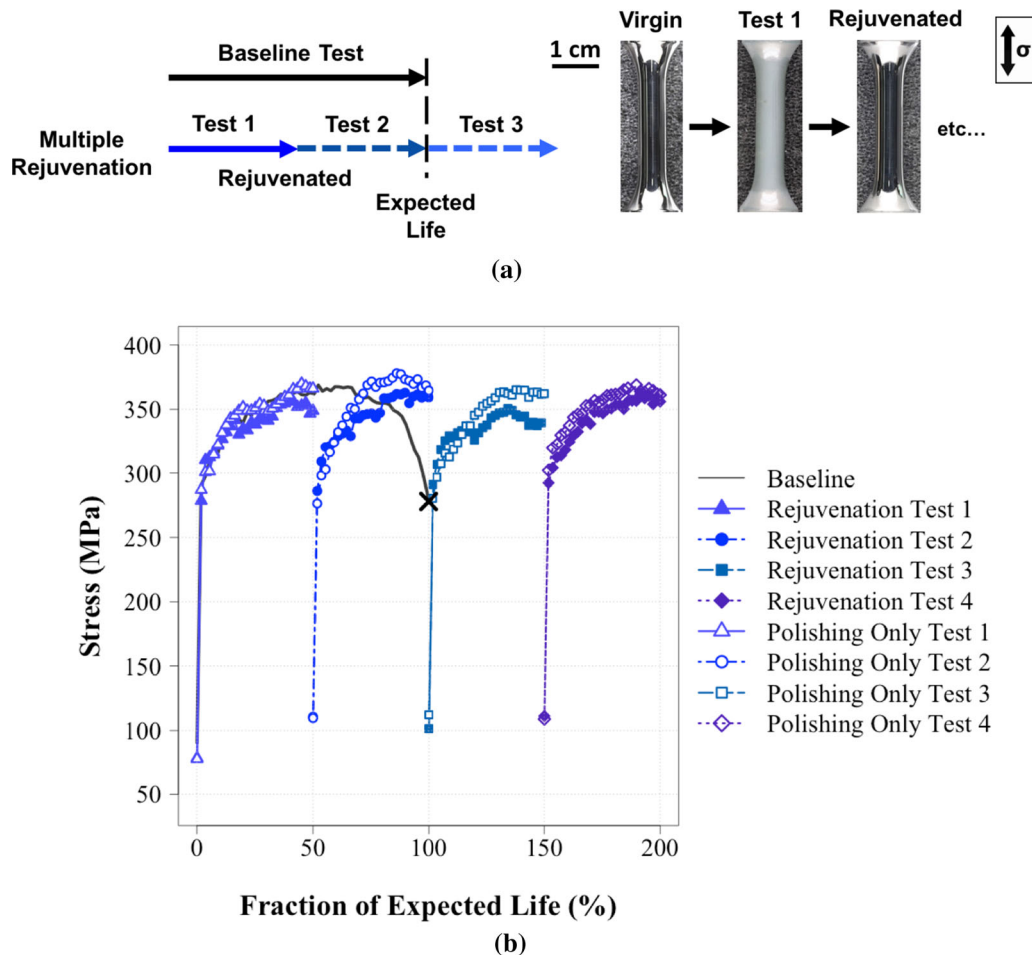


Fig. 18—A summary of the SPLCF multiple rejuvenation test results: (a) a schematic of the hypothesized result is shown along with images of a specimen at various steps of the process. (b) A plot of the maximum stress in a cycle versus fraction of expected life shows that a specimen that is only polished performed similarly to a specimen that was polished and heat treated.

## VII. CONCLUSIONS

Based on the experimental results of multiple rejuvenation testing presented herein, several conclusions are made addressing the questions posed in the introduction:

- A rejuvenation treatment was successfully developed to recover hold-time fatigue of René N5(SX), and creep damage of both GTD444(DS) and René N5(SX). For fatigue damage, only the removal of fatigue cracks was required in order to extend fatigue life, indicating that crack growth is controlled by surface plasticity, defects such as surface undulations and oxide cracks, and oxidation. Testing of coated specimens is warranted in future work to determine if oxidation-assisted crack growth resistance coatings enable rejuvenation via strip and re-coat rather than substantial substrate material removal.
- A critical creep strain threshold of between 3 and 5 pct strain exists for successful heat-treatment-only rejuvenation of René N5(SX). The critical total

creep strain before the introduction of irreversible damage varied depending on the material, creep strain threshold, and solution temperature employed during rejuvenation heat treatment. Full recovery of the creep performance was not attainable through rejuvenation even with a solution heat treatment at the  $\gamma'$  solvus. This is likely a result of heterogeneous deformation due to stress concentrators in the microstructure and the inherent recovery mechanisms in nickel-base alloys.

- Recrystallization was the final life-limiting failure mechanism for a majority of the multiple rejuvenation creep tests performed. However, by reducing the solution temperature, recrystallization can be delayed and, by applying a coating, even suppressed. With a coating, the nucleation of recrystallization at the surface of the superalloy substrate became less favorable due to the elimination of the free surface. In addition,  $\beta$ -NiAl-coated René N5(SX) creep specimens did not contain a  $\gamma'$  depletion zone due to oxidation.

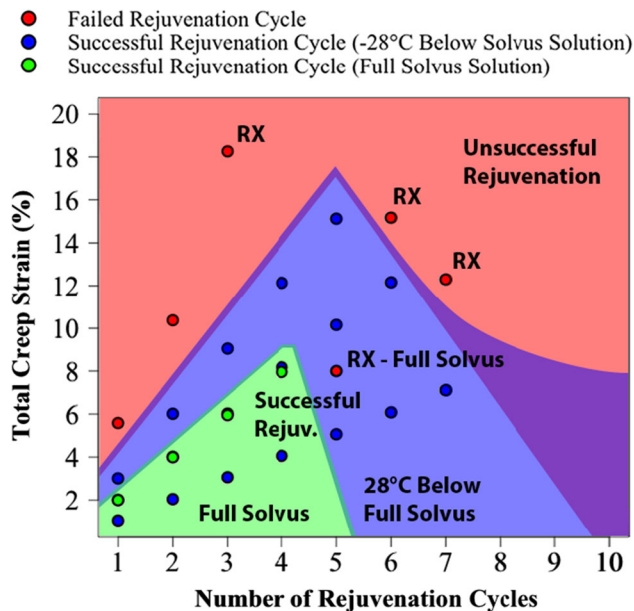


Fig. 19—A René N5(SX) multiple rejuvenation testing map of total creep strain versus number of rejuvenation cycles with the regions of unsuccessful (red) and successful (blue and green) rejuvenation indicated. Only creep tests with at least 80 pct recovery of the original time to the creep strain threshold after rejuvenation were considered successful. The successful rejuvenation region is subdivided into two areas depending on the solution temperature, as indicated. This map is based on a limited number of experimental tests (corresponding to N5-FS-2, N5-28-2, N5-28-3, N5-28-5, and a 1 pct creep strain threshold multiple rejuvenation test) and the regions of uncertainty are indicated in purple. The rejuvenation cycle when recrystallization occurred has also been labeled for each test (Color figure online).

## ACKNOWLEDGMENTS

The authors would like to thank GE Power & Water, specifically Art Peck and Jon Schaeffer, for providing financial support for this work and Chris Torbet for technical support. The RUS measurements were collected using a setup provided by Vibrant NDT Corporation. This work was also supported by the U.S. Air Force Research Laboratory (AFRL) through Research Initiatives for Materials State Sensing (RIMSS) Contract FA8650-15-C-5208, through Universal Technology Corporation. Support of the microscopy equipment is provided by the MRSEC program of the National Science Foundation under Award No. DMR 1121053.

## REFERENCES

1. R. Hart and H. Gayter: *J. Inst. Metals*, 1968, vol. 96, pp. 338–44.
2. J. Dennison, P. Holmes, and B. Wilshire: *Mater. Sci. Eng.*, 1978, vol. 33, pp. 35–47.
3. R. Stevens and P. Flewitt: *Mater. Sci. Eng.*, 1981, vol. 50, pp. 271–84.
4. M. Mclean, H. Tipler, in: Proc. Fifth Symposium on Superalloys, ASM, Materials Park, OH, Superalloys 1984, pp. 73–82.
5. M. D. Ross, G. T. Bennett, D. C. Stewart, Rejuvenation of Turbine Blade Material by Thermal Treatment., Technical Report, DTIC Document, 1979.

6. J. Wortmann: *Mater. Sci. Technol.*, 1985, vol. 1, pp. 644–50.
7. T. Maccagno, A. Koul, J.-P. Immarigeon, L. Cutler, R. Allem, and G. L'espérance: *Metall. Trans. A*, 1990, vol. 21A, pp. 3115–25.
8. E. Lvova: *J. Mater. Eng. Perform.*, 2007, vol. 16, pp. 254–64.
9. W. McCall: *Combustion*, 1971, vol. 42, p. 27.
10. M. Lamberigts, C. Lecomte-Mertens, P. Vierset, in: Application of Advanced Material for Turbomachinery and Rocket Propulsion.
11. B. Rutttert, D. Bürger, L.M. Roncery, A.B. Parsa, P. Wollgramm, G. Eggeler, and W. Theisen: *Mater. Des.*, 2017, vol. 134, pp. 418–25.
12. Z. Yao, C.C. Degnan, M.A. Jepson, and R.C. Thomson: *Metall. Mater. Trans. A*, 2016, vol. 47A, pp. 6330–38.
13. J. Kuipers, K. Wiens, B. Ruggiero, in: ASME Turbo Expo 2017: Turbomachinery Technical Conference and Exposition, American Society of Mechanical Engineers Digital Collection.
14. T.M. Pollock and S. Tin: *J. Propul. Power*, 2006, vol. 22, pp. 361–74.
15. V.K. Tolpygo and D. Clarke: *Acta Mater.*, 2004, vol. 52, pp. 5115–27.
16. J. Nychka and D. Clarke: *Oxid. Met.*, 2005, vol. 63, pp. 325–52.
17. A. Evans, M. He, A. Suzuki, M. Gigliotti, B. Hazel, and T. Pollock: *Acta Mater.*, 2009, vol. 57, pp. 2969–83.
18. T.M. Pollock, B. Laux, C.L. Brundidge, A. Suzuki, and M.Y. He: *J. Am. Ceram. Soc.*, 2011, vol. 94, pp. 136–45.
19. R. Hoefl, E. Gebhardt, Heavy-duty gas turbine operating and maintenance considerations, Technical Report, GE Energy Services, 2000.
20. L. Rettberg, M. Tsunekane, and T. Pollock: *Superalloys*, 2012, vol. 2012, pp. 341–49.
21. P. Callahan, J. Simmons, and M. De Graef: *Modell. Simul. Mater. Sci. Eng.*, 2012, vol. 21, p. 015003.
22. J. MacSleynne, J. Simmons, and M. De Graef: *Modell. Simul. Mater. Sci. Eng.*, 2008, vol. 16, p. 045008.
23. J. MacSleynne, J. Simmons, and M. De Graef: *Acta Mater.*, 2008, vol. 56, pp. 427–37.
24. L. Rettberg and T. Pollock: *Acta Mater.*, 2014, vol. 73, pp. 287–97.
25. L. Rettberg, B. Goodlet, and T. Pollock: *NDT&E Int.*, 2016, vol. 83, pp. 68–77.
26. R. Bürgel, P. Portella, J. Preuhs, in: Proc. 12th Symposium on Superalloys, ASM, Materials Park, OH, Superalloys (2000), pp. 341–49.
27. R.C. Reed: *The Superalloys: Fundamentals and Applications*, Cambridge University Press, Cambridge, 2006.
28. D.B. Miracle and R. Darolia: *Intermetallic Compd.*, 2000, vol. 2, pp. 53–72.
29. M. Pomeroy: *Mater. Des.*, 2005, vol. 26, pp. 223–31.
30. M. Zagula-Yavorska, M. Wierzbińska, K. Gancarczyk, J. Sieniawski, *J. Microsc.* (2016).
31. J. Nystrom, T. Pollock, W. Murphy, and A. Garg: *Metall. Mater. Trans. A*, 1997, vol. 28A, pp. 2443–52.
32. B. Goodlet, C. Torbet, E. Biedermann, L. Jauriqui, J. Aldrin, and T. Pollock: *Ultrasonics*, 2017, vol. 77, pp. 183–96.
33. A. Baldan: *J. Mater. Sci.*, 1991, vol. 26, pp. 3409–21.
34. M. Lafata, L. Rettberg, M. He, and T. Pollock: *Metall. Mater. Trans. A*, 2018, vol. 49A, pp. 105–16.
35. F.R.N. Nabarro and F. De Villiers: *Physics of Creep and Creep-resistant Alloys*, CRC Press, Boca Raton, 1995.
36. T. Pollock and R. Field: *Dislocat. Solids*, 2002, vol. 11, pp. 547–18.
37. D. Cox, B. Roebuck, C. Rae, and R. Reed: *Mater. Sci. Technol.*, 2003, vol. 19, pp. 440–46.
38. G. K. Bouse, M. F. Henry, J. C. Schaeffer, et al., Nickel base superalloys and turbine components fabricated therefrom, 2005. US Patent 6,908,518.
39. E. W. Ross, C. S. Wukusick, W. T. King, Nickel-based superalloys for producing single crystal articles having improved tolerance to low angle grain boundaries, 1995. US Patent 5,399,313.
40. C. S. Wukusick, L. Buchakjian Jr, Nickel-base superalloys, 1991. Patent Number GB 2235697.

**Publisher's Note** Springer Nature remains neutral with regard to jurisdictional claims in published maps and institutional affiliations.